Effect of a Sinusoidal Three-Lobe Total Pressure Distortion on a Transonic Compressor: *Distortion Propagation, Compressor Performance, and Blade Passage Events*

by

Brenda Brennan MacLeod

B. S., Mechanical Engineering (1995)

University of Florida

Submitted to the Department of Aeronautics and Astronautics
in partial fulfillment of the requirements for the degree of
Master of Science in Aeronautics and Astronautics

at the

Massachusetts Institute of Technology

February 2003

Signature of Author ....
Department of Aeronautics and Astronautics
October 31, 2002

Certified by ....
Choon S. Tan
Senior Research Engineer
Thesis Supervisor

Certified by ....
Eugene E. Covert
T. Wilson Professor Emeritus
Thesis Supervisor

Accepted by ....
Edward M. Greitzer
H. N. Slater Professor
Chair, Department Committee on Graduate Students

EFFECT OF A SINUSOIDAL THREE-LOBE TOTAL PRESSURE DISTORTION ON A TRANSONIC COMPRESSOR:
Distortion Propagation, Compressor Performance, and Blade Passage Events

by

BRENDA BRENNAN MACLEOD

Submitted to the Department of Aeronautics and Astronautics
on October 31, 2002, in partial fulfillment of the requirements for the degree of
Master of Science in Aeronautics and Astronautics.

ABSTRACT

This thesis presents data and analysis on compressor performance, distortion propagation, and unsteady blade aerodynamics and structural response when the ADLARF (Augmented Damping of Low Aspect Ratio Fan) compressor is subjected to a sinusoidal, three-lobe (3/Rev) total pressure distortion. The experimental data came from ADLARF tests carried out at engine speeds just above and below the 3/Rev crossing with the first rotor blades' first flex (1F) resonance frequency. The data include pressure and temperature rake data at various axial locations in the flow path of the compressor, static pressure data along the casing and hub walls, laser doppler velocimetry (LDV) data in the blade passages of the first rotor, and differential pressure and strain gauge data at selected locations on selected first rotor blades. As a complementary effort to the distortion propagation analysis, a three-dimensional, unsteady model of the NASA Stage 35 transonic compressor stage was subjected to a sinusoidal 3/rev total pressure distortion. In the analysis of blade aerodynamics and structural response, three-dimensional Navier-Stokes calculations of the ADLARF first rotor subjected to a 3/rev distortion were compared with the LDV data. Three main observations can be made regarding the propagation of the distortion through the compressor: (1) amplification of the total pressure distortion across each rotor, (2) existence of static pressure non-uniformities at the rotor exits with amplitudes of the order of the upstream dynamic pressure, and (3) low pass filter behavior of the compressor stages. Regarding the impact of the distortion on compressor performance, two main observations can be made: (1) an improvement in stall margin and (2) minimal change in performance despite a shift in the operability range. Regarding distortion induced unsteady blade aerodynamics and structural response, three main observations can be made: (1) evidence of excitation of a 16-blade resonance mode in the first rotor and (2) the need for more extensive blade measurements for accurate force and response analysis.

Thesis Supervisors: Choon Tan, Senior Research Engineer
Eugene Covert, T. Wilson Professor Emeritus
Department of Aeronautics and Astronautics

ACKNOWLEDGEMENTS

I am extremely fortunate and grateful for the friends and acquaintances that I have made during this research. It is truly the people involved who have made my experience rich and who have taught me more than just the technical.

For their guidance, support, and patience, I would like to thank my thesis advisors, Dr. Choon Tan and Professor Eugene Covert.

My coursework and thesis were sponsored by the Air Force Research Laboratory at Wright Patterson Air Force Base (AFRL-WPAFB) through the Battelle Memorial Institute with Ms. Pam Teets as the technical officer (Purchase Orders 166212 and 153616) and also through NASA grant #NAG3-2321 with George Stefko as the technical monitor. I am indebted to Dr. Douglas Rabe, Mr. Carl Williams, Mr. John Stauffer, Dr. James Kenyon, Dr. Ronald Fost, and Mr. Brendhan Goss, all of AFRL-WPAFB, for providing me with advice, data, and background information. Likewise, I am indebted to Dr. Steve Manwaring of General Electric Aircraft Engines (GEAE) for providing experimental data and to Dr. Chunill Hah of the National Aeronautics and Space Administration Glenn Research Center (NASA-GRC) for providing his Navier-Stokes calculations. For providing his unsteady Euler code and technical assistance, I am grateful to Dr. Yifang Gong of the MIT Gas Turbine Laboratory. Also, I am grateful to Mr. Neil Murray for his technical assistance with flow visualization software.

For their technical comraderie during my tenure at the Gas Turbine Laboratory, I would like to thank Mr. Jun Luo, Mr. Borislav Sirakov, Mr. Emmanuel Blanvillain, Mr. Vincent Sidwell, and Mr. Vai Man Lei.

For always making administrative issues easier, I would like to thank Ms. Lori Martinez, Ms. Julie Finn, Ms. Holly Anderson, Ms. Mary McDavitt, and Ms. Susan Parker.

Last, but not least, I would like to thank…

…My family at the lab—Beilene, Dongwon, and Jun

…My husband, Bruce, for allowing me to uproot him and for being my inspiration.

TABLE OF CONTENTS

NOMENCLATURE

Acronyms and Abbreviations

"	inches
1/rev	One-lobe or first engine order
1F	First Flex mode
2/rev	Two-lobe or second engine order
2F-1T	Second Flex mode and First Torsion mode
1-2S	Two-Stripe mode
3/rev	Three-lobe or third engine order
8/rev	Eight-lobe or eighth engine order
12/rev	Twelve-lobe or twelfth engine order
ADLARF	Augmented Damping of Low Aspect Ratio Fans
AFRL	Air Force Research Laboratory
AIAA	American Institute of Aeronautics and Astronautics
ASME	American Society of Mechanical Engineers
CRF	Compressor Research Facility
CRFER	Compressor Research Facility Experimental Rig
EO	Engine Order
ft	feet
GEAE	General Electric Aircraft Engines
GRC	Glenn Research Center
GTL	Gas Turbine Laboratory
HCF	High Cycle Fatigue
in	inches
kHz	one thousand cycles per second
ksi	one thousand pounds per square inch
lb	pounds
LDV	Laser Doppler Velocimetry
MIT	Massachusetts Institute of Technology
NASA	National Aeronautics and Space Administration
NOL	Nominal Operating Line
NS	Near Stall
pdyn0	dynamic pressure at the bellmouth
PE	Peak Efficiency
RANS	Reynolds-averaged Navier-Stokes
rev	revolution
rpm	revolutions per minute
s	seconds
WOD	Wide Open Discharge
WPAFB	Wright Patterson Air Force Base

Symbols – Main Text

b	slope of line between two operating points on a pressure ratio curve
c_{ax}	chord length in the axial direction
c_p	specific heat at constant pressure
F	blade force
f_R	reduced frequency
γ	specific heat ratio
M	Mach number
M_r	Relative Mach number
N	mechanical rotation speed of the rotor
N_d	number of distortion cycles per rotor revolution
p	static pressure
p_t	total pressure
θ_F	force phasing
θ_R	response phasing
ρ	density
R	gas constant
r	radius
T	static temperature
T_t	total temperature
V	velocity
V_{ax}	estimated average axial velocity at the inlet to the first rotor
W	work

Symbols – Appendix A

C	constant
d	grid wire diameter
F	constant
f	frequency
G	constant
H	constant
I	constant
J	constant
K	constant
Λ_x	x-direction macro-scale turbulence component
λ_x	x-direction micro-scale turbulence component
Λ_y	y-direction macro-scale turbulence component
λ_y	y-direction micro-scale turbulence component
Λ_z	z-direction macro-scale turbulence component
λ_z	z-direction micro-scale turbulence component
v	fluid kinematic velocity
$R(T)$	autocorrelation function
R_d	Reynolds number
T	autocorrelation time delay

t	time
T_u	x-component turbulence intensity
U	mean flow velocity (in the x-direction).
u^2	x-component of the mean square fluctuating velocities

Symbols – Appendix B

f_s	distortion screen rotation frequency
l_t	distance between distortion screen and compressor inlet
θ_d	angular wavelength of distortion
τ_c	time scale of flow convection from distortion screen to compressor inlet
τ_d	time scale of distortion rotation
U_0	average flow velocity at the bellmouth

Symbols – Appendix C

ETA	overall efficiency
ETAS1	Stage 1 efficiency
N	mechanical rotation speed of the rotor
NC2	corrected rotor speed
PNC2	percent corrected speed
PR	overall total pressure ratio
PRS1	Stage 1 total pressure ratio
PS10	static pressure at the bellmouth
PS15	static pressure at the compressor inlet
PS23	static pressure (axial array) on the casing and hub at the compressor exit
PS23O	static pressure (circumferential array) on the casing and hub at the compressor exit
PSR1L	static pressure on the casing at the Rotor 1 leading edge
PSR2	static pressure on the casing over Rotor 2
PSS1	static pressure on the casing and hub along Stator 1
PSS1L	static pressure on the casing and hub at the Stator 1 leading edge
PSS1T	static pressure on the casing and hub at the Stator 1 trailing edge
PSS2L	static pressure on the casing and hub at the Stator 2 leading edge
PSS2T	static pressure on the casing and hub at the Stator 2 trailing edge
PT10	total pressure at the bellmouth
PT15	total pressure at the compressor inlet
PT23	total pressure at the compressor exit
PTS1	average total pressure at the Stator 1 leading edge
PTS1L	total pressure at the Stator 1 leading edge
PTS2L	total pressure at the Stator 2 leading edge
S1POS	Stator 1 vane position
SCRNANG	rotation angle of the distortion screen
TR	overall total temperature ratio
TRS1	Stage 1 total temperature ratio
TT00	total temperature exiting the flow conditioning elements
TT23	total temperature at the compressor exit

TTS1	average total temperature at the Stator 1 leading edge
TTS1L	total temperature at the Stator 1 leading edge
TTS2L	total temperature at the Stator 2 leading edge
WAV31C	corrected mass flow rate

Symbols – Appendix C

A_H	area of the high-speed segment
A_L	area of the low-speed segment
b	slope of line drawn between the high- and low-speed performance points
C	positive coefficient
Δ	(non-normalized) vertical drop along total-to-static pressure rise curve
π_H	pressure ratio for the high-speed segment
π_L	pressure ratio for the low-speed segment
p_{2H}	static pressure in high-speed segment at compressor or stage exit
p_{2L}	static pressure in low-speed segment at compressor or stage exit
p_{t1H}	total pressure in high-speed segment at compressor or stage inlet
p_{t1L}	total pressure in low-speed segment at compressor or stage inlet
p_{t2H}	total pressure in high-speed segment at compressor or stage exit
p_{t2L}	total pressure in low-speed segment at compressor or stage exit

Chapter 1

INTRODUCTION

The blading in turbomachinery is subject to a wide variety of vibrations due to the combination of geometry configuration, high rotating speeds, and unsteady and non-uniform flow conditions. Blade vibrations, which can become amplified at resonance frequencies, are of critical concern to turbomachinery durability and safety since vibrations can cause high cycle fatigue (HCF) failures. While engineers have relatively good control over geometry and operational parameters, they have much less control over flow non-uniformities and the unsteadiness of the resulting flow in aircraft turbine engines.

In aircraft turbine engines, non-uniform flow conditions, which may or may not involve vortices, can result from many sources, including inlet distortions and wakes. Inlet distortions result from the ingestion of turbulence, jet exhaust, separation of the flow at the nacelle lip (due to angle of attack and slip angle), and flow separation inside the inlet duct. Wakes result from upstream obstructions, such as rotors, struts, and stators. Distortions in total temperature can be caused by re-ingestion of jet exhaust while distortions in total pressure can be caused by all of the items listed above. This thesis, however, limits its focus to total pressure distortions and their role in causing turbomachinery blades to vibrate.

1.1 Background on the ADLARF Testing

A series of experiments was carried out by the Air Force Research Laboratory (AFRL) at Wright Patterson Air Force Base (WPAFB) and General Electric Aircraft Engines (GEAE) in the 1990s in order to study the forced response of compressor blades subjected to total pressure distortions. The programs included steady and unsteady measurements of blade response in the ADLARF (Augmented Damping of Low Aspect Ratio Fan) compressor. The compressor was tested in the Compressor Research Facility Experimental Rig (CRFER), and a variety of distortions screens were used far upstream of the compressor to create different shaped total pressure distortions. The different distortion screens had both circumferential and combined circumferential/radial patterns. It is the circumferential distortion that subjects the blades to the cyclic flow conditions which drive the blade vibrations. Testing was done at or near the appropriate resonance frequencies in order to capture the conditions of concern to HCF. For practical reasons (i.e., survivability of the instrumentation), all data taken at resonance were obtained while accelerating or decelerating through resonance. The data taken near resonance, however, were taken at constant mechanical rotation speeds.

Most of the testing was done using distortion screens with two-, three-, and eight-lobe circumferential patterns. In a rotor reference frame, this corresponds to 2/, 3/, and 8/rev flow distortions, respectively, which correspond to forcing frequencies of the 2nd, 3rd, and 8th engine orders (EO), respectively. The Campbell diagram of the ADLARF compressor first rotor is shown in Figure 1-1. It shows the frequency of the engine orders as a function of rotation speed as well as the resonance frequencies of the various blade vibration modes as a function of rotation speed.

One can see that the blades will be driven at a resonance frequency at rotation speeds where the forcing frequency EO crosses a resonance mode frequency. The resonance crossings studied with the 2/, 3/, and 8/rev distortion screens are the first flex (1F), the second flex – first torsion (2F-1T), and the first two-stripe (1-2S) modes.

In addition to other flow measurements, data were taken to delineate flow in the blade passage and to determine pressures and strains on the first rotor blades. Blade passage flow was measured using laser doppler velocimetry (LDV) at the 85% span and at the leading and trailing edge planes. Depending on the measurement configuration, gauge or differential pressure was measured using kulites mounted in through-holes along the 85% span. Blade strain was measured by strain gauges mounted at locations of resonance mode bending.

A number of studies were published based on the above measurements. The inlet distortion was defined using total pressure rakes at the compressor inlet [1]. The steady and unsteady blade passage flow fields were defined and blade passage events were identified using LDV data [2,3]. Unsteady gauge pressure measurements along the blade chord were decomposed and analyzed for frequency content and disturbance propagation speed [4]. Steady and unsteady models of blade passage flow were assessed and validated using rake, LDV, and kulite data [1,2,3,5]. Blade forces and moments were calculated from differential blade pressure measurements along the blade chord [6,7]. Through analyses of strain gauge measurements, the role of mistuning in the distribution of vibration amplitude among the blades was investigated, resulting in an initial assertion of aerodynamic coupling [8,9] and a later assertion of structural coupling [10]. In addition, reduced order models of coupled aeromechanics were used to investigate forced response [5,8,9].

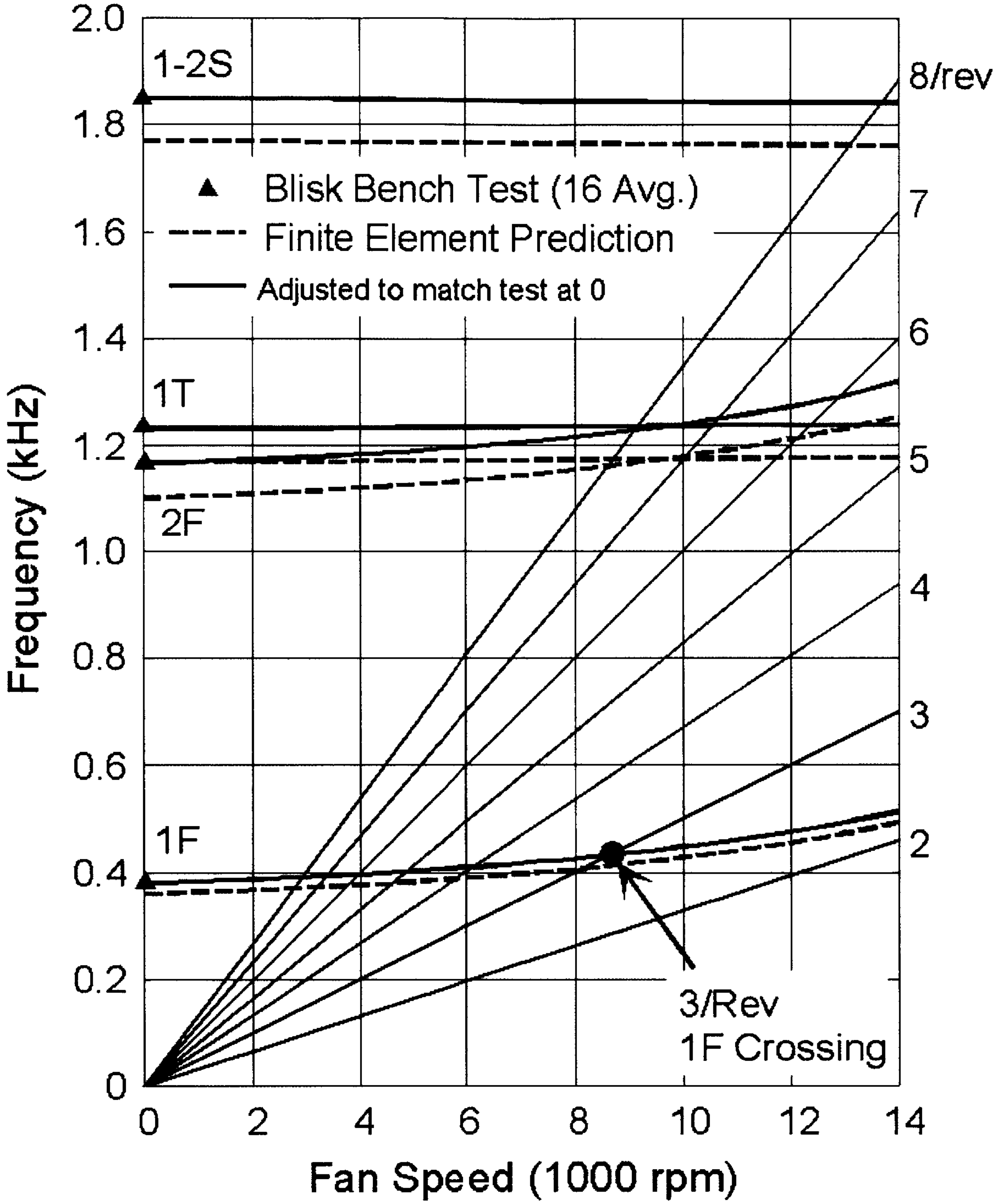

Figure 1-1. Blade resonance frequencies and engine order frequencies versus compressor speed for the ADLARF first rotor. (Courtesy AFRL-WPAFB)

Although much analysis has been done on the ADLARF data sets, a quantitative link from inlet distortion to blade vibration has not yet been established. The weakest links in the understanding are the blade-to-blade variations and the coupling of blades to the flow field and to each other. Qualitatively, it is understood that a circumferential total pressure distortion, incident on a rotor, will cause oscillations in the blade loading, which will amplify the blade vibrations if the oscillations are at one of the lower resonance frequencies. Quantitatively, the flow field for steady inlet flow is well defined for the ADLARF first rotor. However, understanding of the coupling that occurs between aerodynamics and blade motion during forced response relies on reduced order models [5,8,9], which are difficult to validate using data from the ADLARF tests.

1.2 Technical Objectives

The current effort seeks to enhance both the qualitative and quantitative understanding of inlet distortion induced blade excitations. The original research questions that motivated this research effort were the following:

(1) How must one design and implement ground tests/experiments to reproduce key aspects of blade excitation seen in flight situations in which the engine encounters a distortion?

(2) How would one parameterize the aerodynamic loads on blades in terms of inlet distortion characteristics and compressor design characteristics?

(3) What sets the extent of the downstream influence of a distortion on blade excitations in a multi-stage compressor?

(4) What would constitute an adequate model (computational or reduced-order type) for addressing blade excitations under inlet distortion?

The first research question could not be addressed due to a lack of resources—data from flight tests is sparse. Turbulence length scales for the distortion screen were estimated (Appendix A), but no flight data were made available for comparison.

Research objectives were then reformulated in an effort to seek answers to the last three questions, which involve the following tasks:

1. Examine the downstream evolution of a distortion through a multi-stage compressor using data from ADLARF tests and a three-dimensional computational model for multi-stage compressors.

2. Determine the aerodynamic loads from selected inlet distortions.

3. Determine distortion-induced blade excitations.

1.3 Contributions

The following contributions result from this research:

1. Acquisition and analysis of data from AFRL-WPAFB and GEAE. System and blade level ADLARF data were analyzed in order to understand the impact of a 3/rev inlet

distortion on a transonic compressor. Examination of distortion propagation, compressor performance, and blade aeromechanics yielded the following key observations:

- Amplification of the total pressure distortion by the compressor rotors.
- Static pressure distortions at the rotor exits with amplitudes of the order of the upstream dynamic pressure.
- Low-pass filter behavior from the rotors.
- Improvement in compressor stall margin and marginal change in compressor pressure ratio and efficiency.
- Shift in compressor operability range.
- Strong circumstantial evidence of the excitation of a 16-blade resonance mode in the rotor.

2. Establishment of an appropriate low-pass corner frequency length scale for low-aspect-ratio compressor rotors.
3. Identification of experimental issues that are obstacles to force and response analysis of rotor blades.

1.4 Thesis Organization

This thesis focuses on experimental and computational results of 3/rev distorted flow through transonic compressors—mainly, the ADLARF compressor. Chapter 2 ("Technical Approach") explains how experimental data and computational results are used in the pursuit of the research objectives. Chapter 3 ("Distortion Propagation") focuses on Objective #1 in an effort to determine the conditions under which an inlet distortion might pose an HCF problem. Chapter 4 ("Compressor Performance") focuses on Objective #2 with respect to the inlet distortion's effect on compressor performance. Chapter 5 ("Blade Aerodynamics and Structural Response") focuses on Objectives #2 and #3 by attempting to determine distortion induced blade passage events and the resulting force and response scenario. Finally, Chapter 6 ("Conclusions") synthesizes the results from the analyses in Chapters 3-5 and presents conclusions on the results, the experimental issues, and future work.

Chapter 2

TECHNICAL APPROACH

This chapter describes the ADLARF experimental data and computational tools that are used in the current effort to investigate the effects of inlet distortions on transonic compressors. The ADLARF data are used extensively to investigate all three main thesis topics—distortion propagation, compressor performance, and blade aerodynamics and structural response. The computational tools that are used consist of a three-dimensional computational model for high-speed, multi-stage compressors developed by Gong [12] and an unsteady three-dimensional Navier-Stokes solver developed by Hah [3]. The former was used to subject NASA Stage 35 to a 3/rev distortion similar to the one seen in the ADLARF data. The latter was used to subject the ADLARF first rotor to a 3/rev inlet distortion. Results from the Stage 35 computation are used to complement the investigation of distortion propagation while results from the ADLARF rotor computation are used mainly to complement the investigation of blade passage aerodynamics.

2.1 The ADLARF Experimental Data

The ADLARF experimental data are the result of a collaboration between the GEAE Advanced Engineering Programs Department and the Wright Laboratory Aeropropulsion and Power Directorate. The particular test configuration of the ADLARF compressor that is of interest consists of two transonic stages without any inlet guide vanes. The corrected design speed of the compressor is 13,288 rpm, and the pressure ratio at design is 4.3. Table 2-1 lists the specifications on the first rotor, which has a diameter of 27.75 inches.

Table 2-1. Rotor 1 Parameters [11].

Number of Blades	16
Aspect Ratio at Root	1.1
Tip Solidity	1.5
Hub Solidity	2.67
Tip Thickness/Chord Ratio	.028
Hub Thickness/Chord Ratio	.087
Material	Ti-6-4

Two different data sets were studied from the ADLARF tests. All data, with the exception of the LDV data, came from tests at 71% of the corrected design speed. The

LDV data came from a 62% design speed test. The 71% speed clean inlet tests were run on December 19, 1996, and the 71% speed 3/rev distortion tests were run on January 7, 1997. All testing took place at the WPAFB Compressor Research Facility (CRF, Figure 2-1). Tip speed and pressure ratio for the 71% design speed tests were approximately 1100 ft/s (335 m/s) and 2.3, respectively.

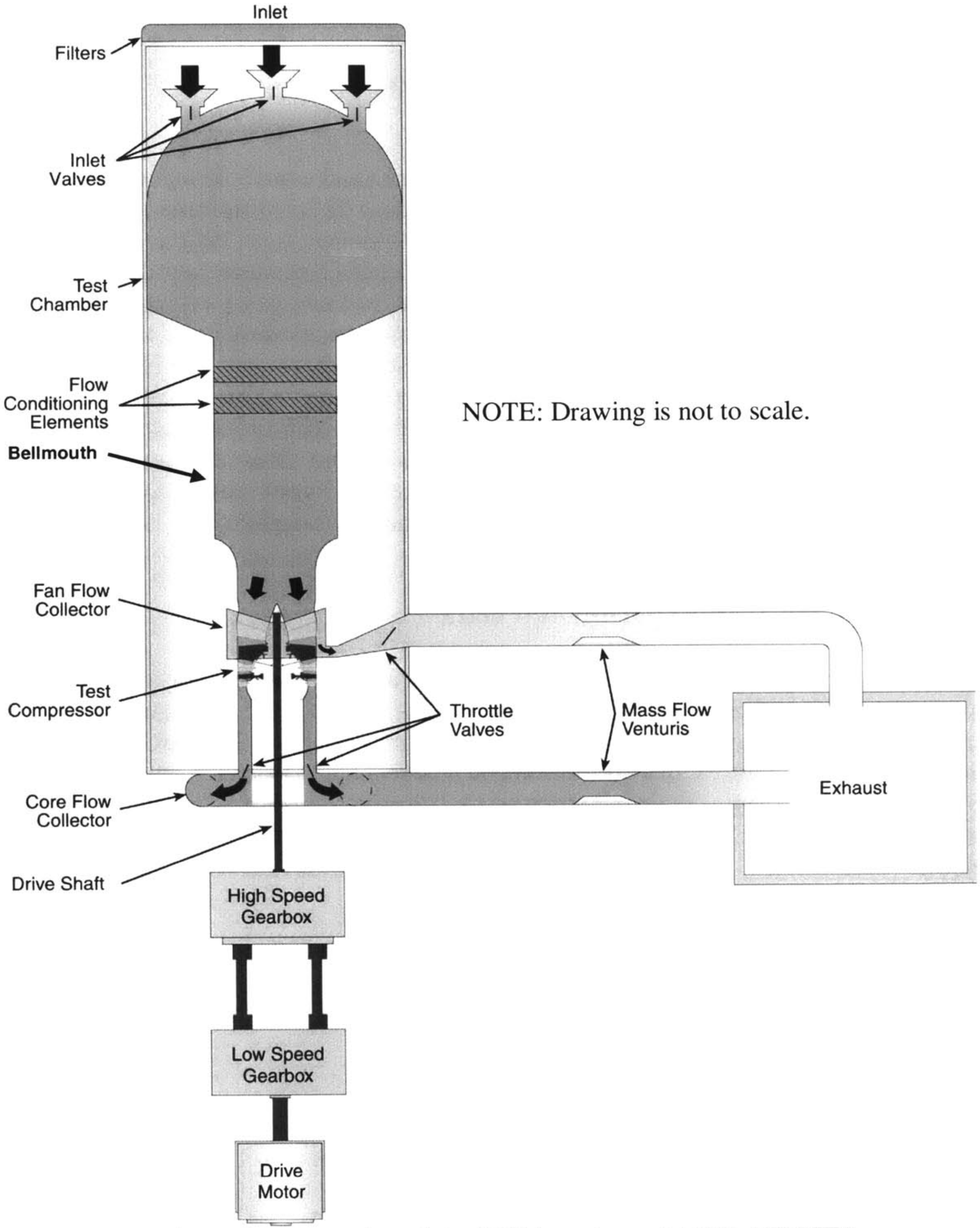

Figure 2-1. Horizontal cross-section of the CRF (courtesy of AFRL-WPAFB).

2.1.1 Test Method

For the 71% speed tests, a clean inlet and a 3/rev inlet distortion were tested at four different compressor operating points. The operating points were near stall (NS), peak efficiency (PE), nominal operating line (NOL), and wide-open discharge (WOD). The NS and PE points were determined during testing, while NOL was set by the compressor design and WOD was set by the facility. Flow rates for the operating points are listed in Table 2-2. Note that there is a small drop in corrected mass flow rate due to the drop in total pressure across the distortion screen.

Table 2-2. Corrected mass flow rate (lb/s) for clean and distorted inlets at the four operating points.

INLET CONDITION	NS	PE	NOL	WOD
Clean	98.5	101.9	103.5	104.1
Distorted	96.8	99.8	101.3	102.0

In the distorted flow tests, a 3/rev screen was placed perpendicular to the flow upstream of the compressor inlet (Figure 2-2). The screen (Figure 2-3) consists of eighteen 20-degree circumferential segments hinged together along the radial edges. The 3/rev distortion pattern is created by alternating 60-degree sections of coarse mesh and fine mesh. The fine mesh sections are further divided by the 20-degree segments, having a very fine segment flanked by less fine segments. The coarse mesh sections are also further divided by the 20-degree segments, having a very coarse segment flanked by less coarse segments. These subdivisions give the distortion its sinusoidal shape. In order to expedite testing and improve data resolution, the distortion screen was rotated at 2 degrees per second, resulting in a temporal as well as spatial disturbance. The screen rotation rate was slow enough, though, that the flow can be assumed to be quasi-steady. (See time-scale calculations in Appendix B.)

2.1.2 Test Measurements

Flow field, differential pressure across the blade (Rotor 1 only), and strain at the blade root (Rotor 1 only) were measured during these particular ADLARF tests. Flow field was measured using pressure and temperature rakes at various axial locations in the flow path of the compressor, static pressure taps along the casing and hub walls, and LDV in the blade passages (Rotor 1 only). Differential pressure across the blade was measured using kulites mounted in through-holes along the 85% span of the blade. Blade strain was measured using strain gauges mounted at the blade root.

The flow field data obtained from total pressure and temperature rakes and from pressure taps are used to investigate distortion propagation and compressor performance. The measurement stations are listed in Table 2-3 along with the figure number that shows their general locations. The stations are listed in the order that the flow encounters them—upstream to downstream. Detailed information on the location and orientation of the rakes and taps is presented in Appendix C.

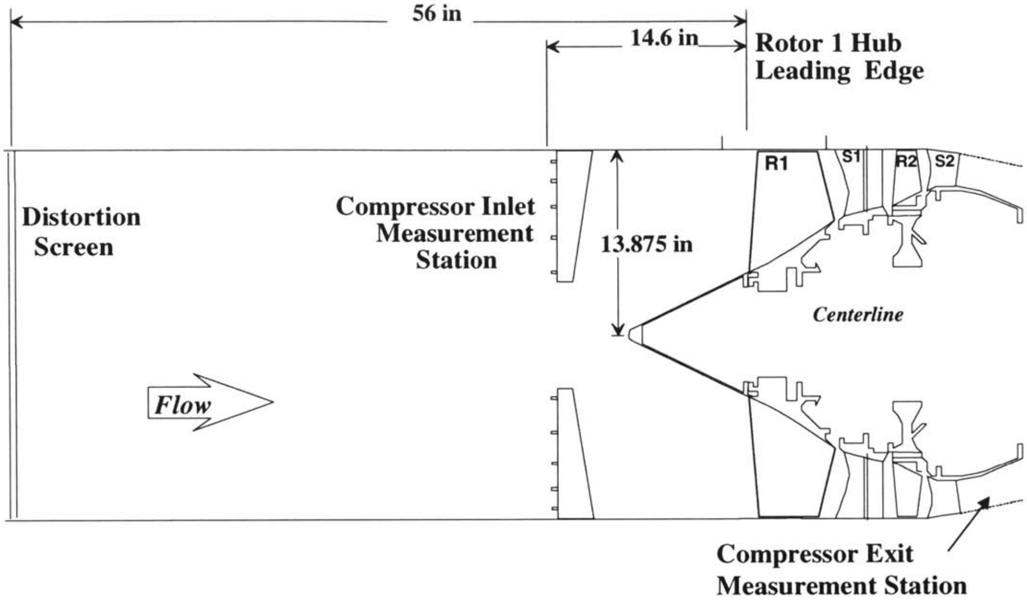

Figure 2-2. Cross-section of the experimental set-up (courtesy of AFRL-WPAFB).

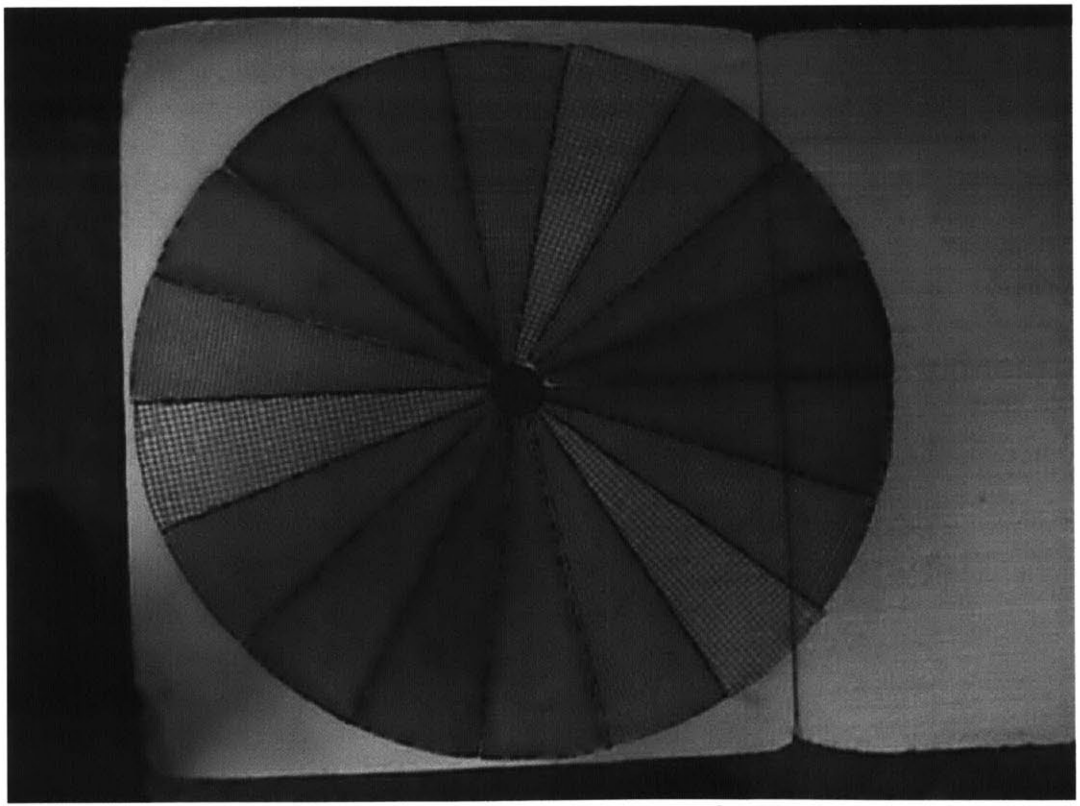

Figure 2-3. Sinusoidal 3/rev distortion screen (courtesy of AFRL-WPAFB).

Table 2-3. Flow field measurement stations.

MEASUREMENT STATION	FIGURE NUMBER
Flow Conditioning Barrel	2-1
Bellmouth	2-1
Compressor Inlet	2-2
Rotor 1 Leading Edge	2-2
Stator 1	2-2
Rotor 2 Tip	2-2
Stator 2	2-2
Compressor Exit	2-2

The LDV measurements are used to investigate blade passage events. The data were taken across the 85% span and across the rotor inlet and exit for distorted flow at 62% design speed. The resolution of the measurement system provided 30 locations across the blade pitch, 21 in the axial direction, and 12 in the radial direction. A minimum of 50 samples were ensemble-averaged for each measurement location [2]. The distortion screen was held stationary at various screen positions in order to get the required samples for ensemble averaging.

Kulite measurements are used to investigate blade force and aerodynamic events along the blade chord. The kulites were mounted in through-holes along the 85% span as shown in Figure 2-4. They were mounted flush with the pressure surface on Blade 1 and flush with the suction surface on Blade 2. Since the holes were open to the other side, measurements yielded differential pressure, which should not reflect differences due to the orientation of the mounting. Note that Blade 2 is ahead of Blade 1 in the rotation.

Strain gauge measurements are used to investigate the response of the blades to the inlet distortion. Strain gauges were mounted at the roots of the blades because that is where maximum bending for the 1F vibration mode occurs.

2.2 The NASA Stage 35 Model

The analysis tool used to complement the investigation of distortion propagation is a three-dimensional unsteady nonlinear Euler flow field model written and configured for the NASA Stage 35 compressor by Gong in 1999 [12]. The computational model was used to simulate rotating stall inception and development as well as inlet distortion propagation through low- and high-speed multi-stage compressors. The model provides a blade row by blade row body force representation of a multi-stage compressor, unsteady three-dimensional flow outside of the blade rows, and work input and flow turning through the body force, which depends on local flow conditions.

For the distortion propagation investigation, a sinusoidal 3/rev total pressure distortion was imposed on a single stage (rotor followed by a stator) transonic compressor model. Some design parameters for the Stage 35 rotor are shown in Table 2-4.

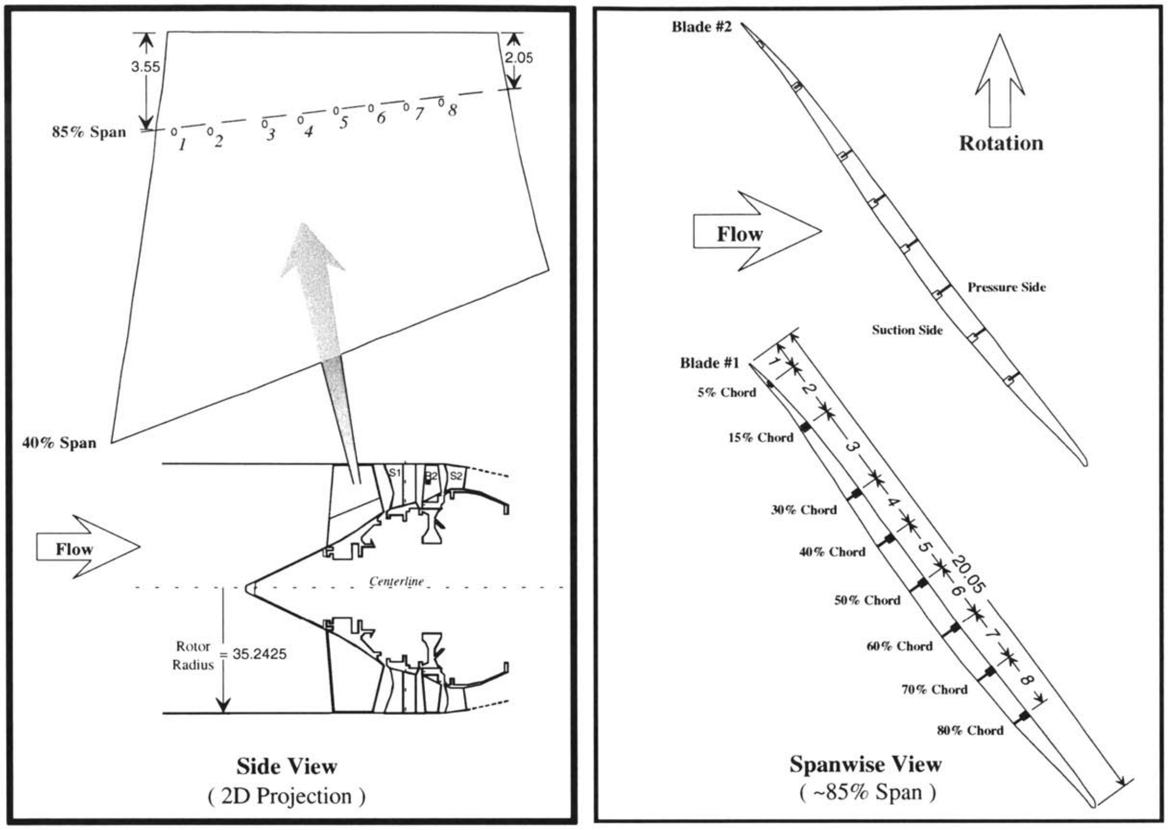

Figure 2-4. Location and orientation of the kulite transducers (courtesy of AFRL-WPAFB).

Table 2-4. Stage 35 Rotor Parameters [12].

Number of Blades	36
Aspect Ratio	1.19
Tip Solidity	1.29
Hub Solidity	1.77
Design Speed	17,200 rpm
Tip Speed at 72% design	1,080 ft/s
Pressure Ratio at 72% design	1.3

As can be seen in the Table 2-4 and in the Section 2.1 introduction, the Stage 35 rotor is similar to the ADLARF first rotor in aspect ratio, tip solidity, and tip speed. The pressure ratio also is within 20% of the ADLARF Rotor 1 pressure ratio at 71% design speed (Figure 4-1). Thus, the Stage 35 model can arguably be used to complement the ADLARF experimental data to some extent, rather than having to extract the body force representation of the ADLARF compressor in order to model it. Such a task would be tedious and of limited benefit as the model is being used to identify and/or confirm physical trends in distortion amplification, static pressure non-uniformities, and induced swirl.

2.3 The RANS Model of the ADLARF First Rotor

The analysis tool used mainly to complement the investigation of blade passage aerodynamics is a Reynolds-averaged Navier-Stokes (RANS) solution of the blade passages of the ADLARF first rotor by Hah *et al* [3]. The total pressure distribution, the total temperature, and two velocity components serve as boundary conditions at the inlet surface. At the exit boundary surface, static pressure is specified at one circumferential location. Since a 3/rev distortion yields no symmetry in a 16-blade rotor, the flow field for the entire rotor was caclulated.

Results from the RANS ADLARF rotor model are used to define the blade passage flow field and identify unsteady events resulting from the inlet distortion. These computational data are at the same rotational speed (71% of design) as the ADLARF experimental data, with the exception of the LDV data. The LDV data were taken at a lower speed (62% of design); however, qualitative comparisons can still be made with the rotor computations because the incident flow is still in the transonic regime. In addition to flow field comparisons, comparisons of distortion propagation and compressor performance parameters are made using the computational data.

2.4 Summary

This chapter presents the technical approach of this research effort. The effort focuses on three main topics—distortion propagation, compressor performance, and blade aerodynamics and structural response. The ADLARF data, which are central to all three topics, are described in terms of test configuration, method, and measurements. A brief decription of the Stage 35 model, which is used to complement the distortion propagation investigation, is presented along with geometry and design specifications from the Stage 35 rotor (Table 2-4). Lastly, a brief description of the RANS ADLARF rotor model, which is used mainly to complement the blade passage aerodynamics investigation, is presented.

Chapter 3

DISTORTION PROPAGATION

This chapter looks at the propagation of a sinusoidal 3/rev total pressure distortion through a transonic compressor. The objective is to determine whether a distortion will be able to pose an HCF problem for rotor blades downstream of the first stage. To this end, this chapter investigates whether a distortion will be attenuated or amplified as it proceeds through a multi-stage compressor.

The first section of the chapter uses equations relating compressible flow properties in order to provide perspective on screen-generated total pressure distortions. Results from the Stage 35 model are also provided to illustrate the distorted flow behavior and to elucidate anticipated local changes in the magnitudes of flow properties due to such total pressure distortions. The second section examines distortion propagation in the ADLARF compressor using experimental data and results from the RANS computation of Rotor 1. The third section uses the computational flow field in the Stage 35 model to corroborate the ADLARF measurements. Finally, the results section focuses in on the two important topics governing distortion propagation: the filtering of frequency components and distortion amplification.

3.1 Anatomy of a Screen-Generated Total Pressure Distortion

This section uses compressible flow relations and the equation of state to examine the anatomy of a screen-generated total pressure distortion. Figures shown were generated using results from the Stage 35 model as it responded to a sinusoidal 3/rev total pressure distortion at 72% of its design speed.

A typical total pressure distortion generated by a screen in an inlet duct implies distortion of other properties as well as of total pressure. For a screen that is far upstream of the compressor, two main assumptions can be made about the flow just after the distortion screen—the streamlines are straight and parallel, and there is negligible heat transfer across the streamlines. These assumptions imply uniform static pressure p and uniform total temperature, respectively.

Using the relationships between stagnation (total) and static quantities in terms of Mach number M, the relation for total and static pressure,

$$p_t = p\left[1+\tfrac{\gamma-1}{2}M^2\right]^{\frac{\gamma}{\gamma-1}}$$

implies high Mach number in areas of high total pressure as well as the converse (Figure 3-1, from the 3/rev distortion imposed on NASA Stage 35 using Gong's three-dimensional computational model for multi-stage compressors). This, together with the relation for total and static temperature,

$$T_t = T\left[1+\tfrac{\gamma-1}{2}M^2\right]$$

then implies low temperature in areas of high total pressure as well as the converse (Figure 3-2). As a result, the equation of state for a perfect gas,

$$p = \rho R T$$

where R is the gas constant, implies high density ρ in areas of high total pressure as well as the converse (Figure 3-3). The definition of Mach number,

$$M = \frac{V}{\sqrt{\gamma R T}}$$

or,

$$V = M\sqrt{\gamma R T} = \sqrt{\frac{2}{\gamma-1}\left[\left(\frac{p_t}{p}\right)^{\frac{\gamma-1}{\gamma}}-1\right]}\sqrt{\frac{\gamma R T_t}{\left(\frac{p_t}{p}\right)^{\frac{\gamma-1}{\gamma}}}} = \sqrt{\frac{2\gamma R T_t}{\gamma-1}\left[1-\left(\frac{p_t}{p}\right)^{\frac{-(\gamma-1)}{\gamma}}\right]}$$

then implies high velocity V in areas of high total pressure as well as the converse (Figure 3-4).

To summarize, the presence of a total pressure distortion in uniform static pressure and total temperature fields requires that there also be distortions in Mach number, static temperature, density, and velocity. The Mach number, density, and velocity distortions are in phase with the total pressure distortion while the static temperature distortion is out of phase. The distortions in Mach number and velocity are intuitive; however, the distortions in density and static temperature may not be. The main deduction that can be made from this analysis is that these distortions result in higher concentrations of mass and momentum in areas of high total pressure.

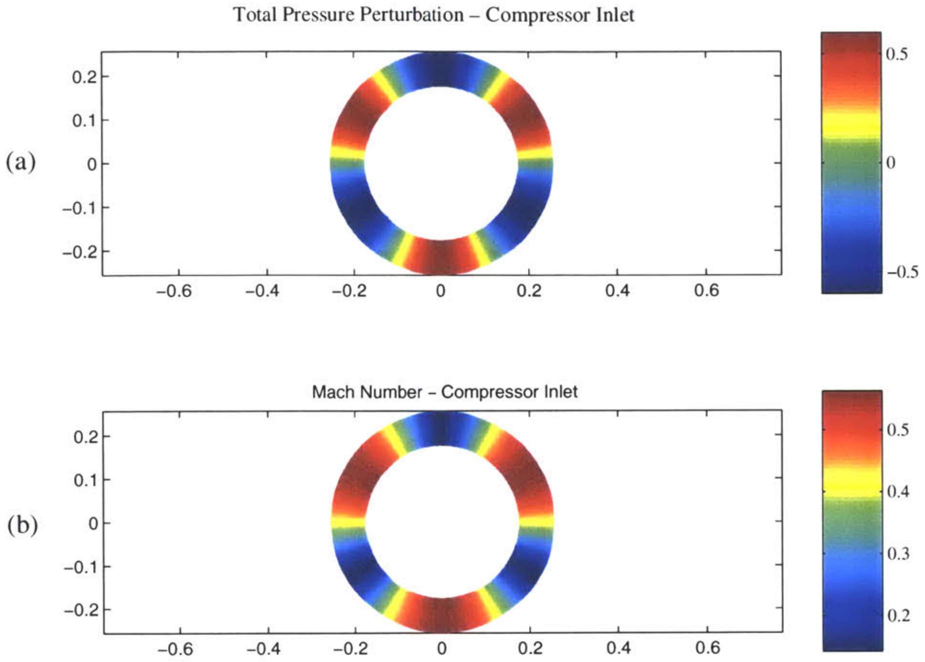

Figure 3-1. (a) Total pressure perturbation normalized by the upstream dynamic pressure and (b) Mach number at the compressor inlet of NASA Stage 35.

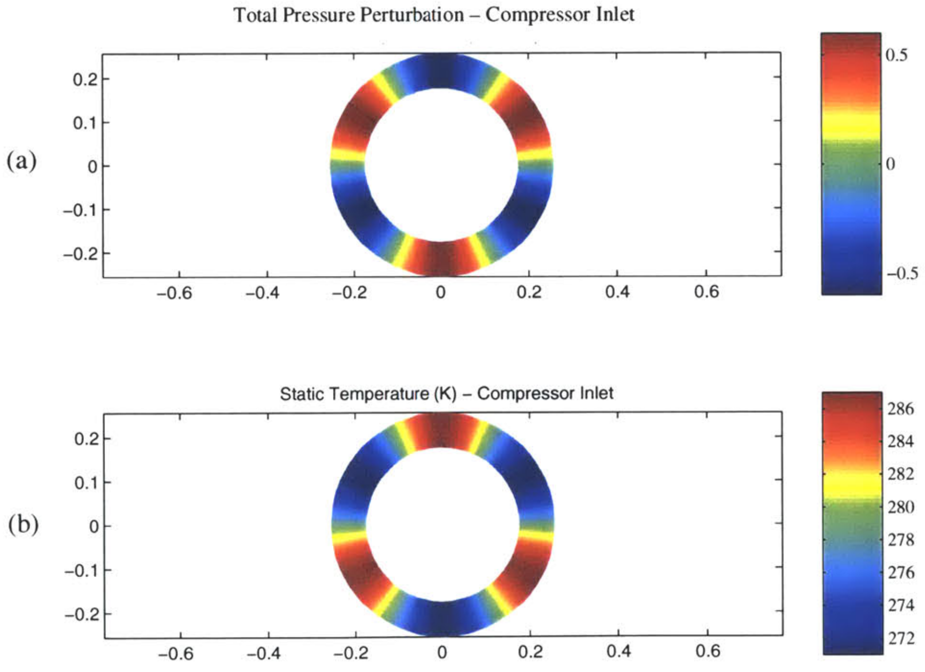

Figure 3-2. (a) Total pressure perturbation normalized by the upstream dynamic pressure and (b) static temperature at the compressor inlet of NASA Stage 35.

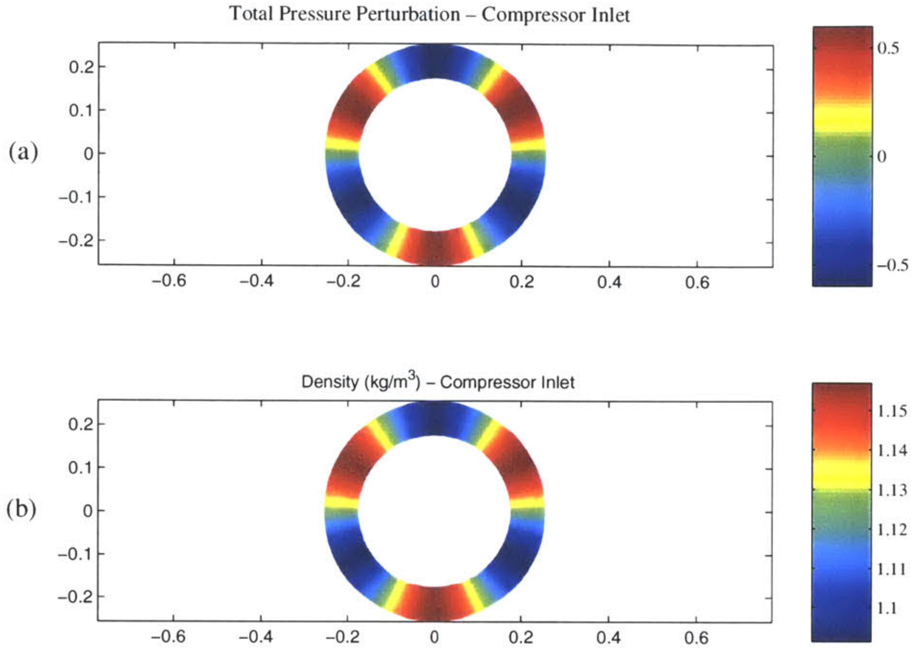

Figure 3-3. (a) Total pressure perturbation normalized by the upstream dynamic pressure and (b) density at the compressor inlet of NASA Stage 35.

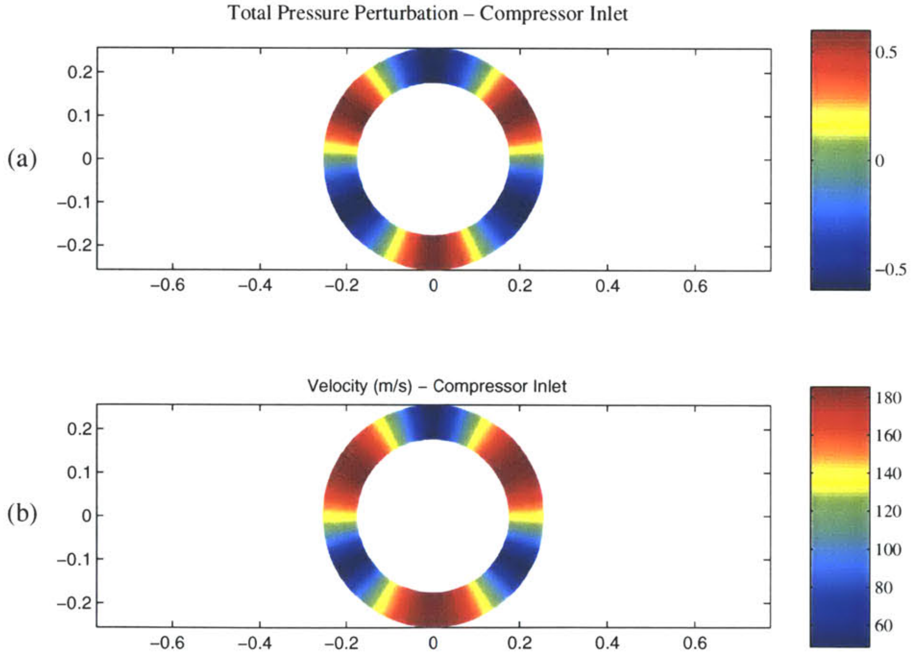

Figure 3-4. (a) Total pressure perturbation normalized by the upstream dynamic pressure and (b) velocity at the compressor inlet of NASA Stage 35.

3.2 Distortion Propagation in the ADLARF Compressor

During the ADLARF tests, a distortion screen was used to create a 3/rev total pressure distortion similar to the one imposed on the Stage 35 model. The propagation of the distortion through the compressor was measured by total pressure rakes at the compressor inlet (located one rotor radius upstream of the Rotor 1 inlet), the Stator 1 leading edge, the Stator 2 leading edge, and the compressor exit (Figure 3-5). Propagation through the RANS model of the ADLARF first rotor is shown in Figures 3-6 and 3-7 for the purposes of comparison.

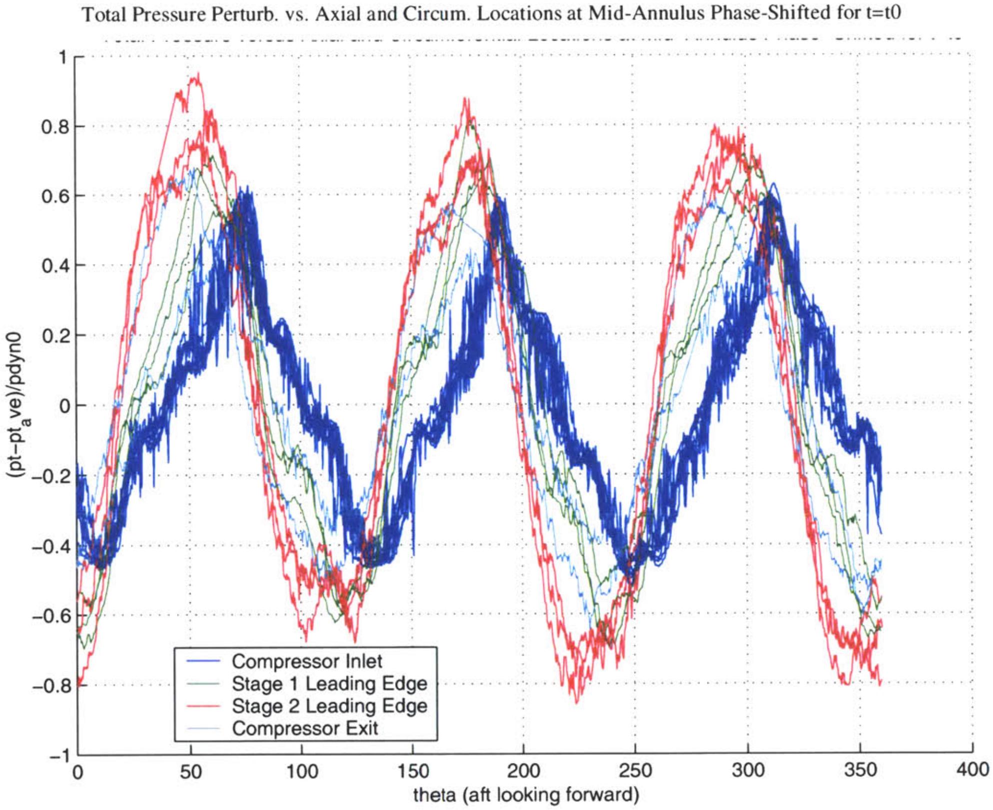

Figure 3-5. ADLARF total pressure perturbation normalized by the average bellmouth dynamic pressure versus circumferential location as measured at each mid-annular sensor.

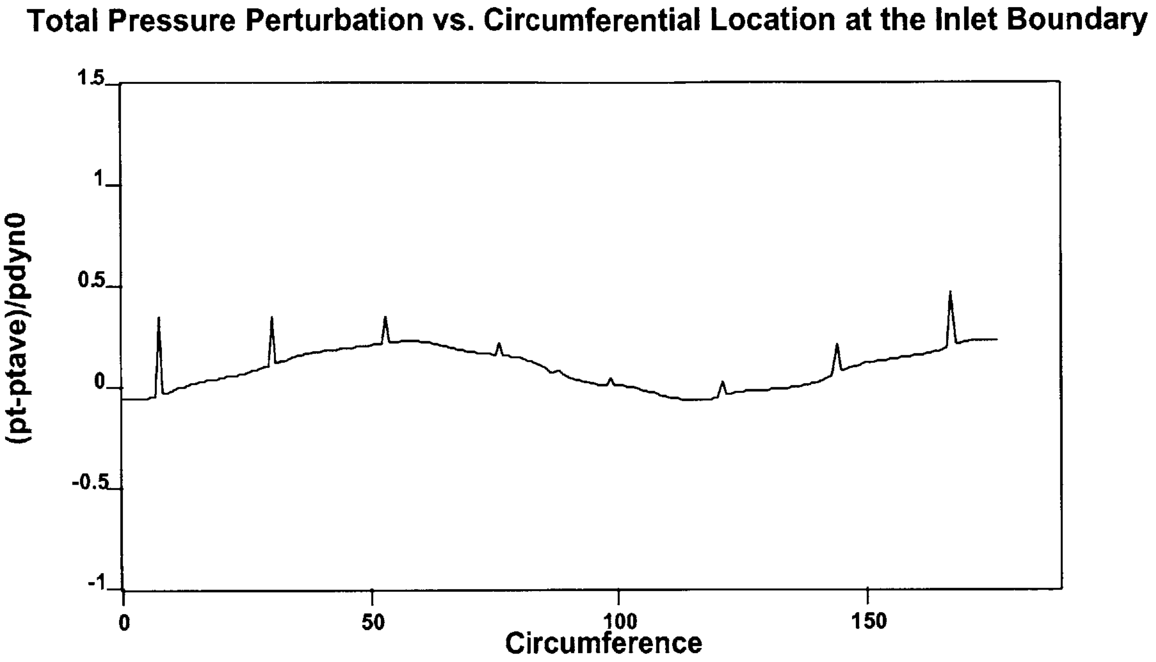

Figure 3-6. Total pressure perturbation normalized by the average inlet dynamic pressure versus circumferential location at 85% span on the ADLARF first rotor computation inlet boundary surface.

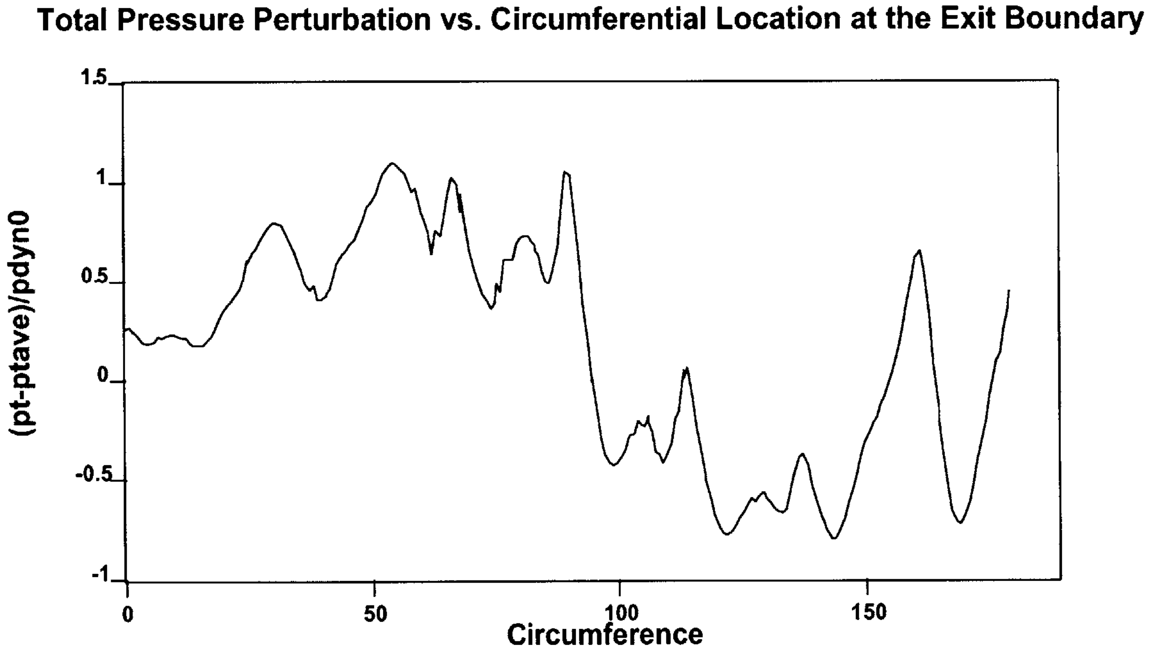

Figure 3-7. Total pressure perturbation normalized by the average inlet dynamic pressure versus circumferential location at 85% span on the ADLARF first rotor computation exit boundary surface.

As seen in Figure 3-5, both rotors amplify the distortion. Results from the RANS rotor computation also show amplification, but the magnitude of the amplification is several times larger than in the experimental data. Thus, the RANS rotor model significantly over-predicts distortion amplification. The small spikes in the RANS total pressure data at the inlet boundary surface correspond, in number and spacing, to the rotor blades. However, there is no physical reason for the blades to cause total pressure disturbances upstream of the rotor. The larger total pressure spikes at the exit boundary surface also reflect the presence of the blades, but it unknown to what extent their existence is physically reasonable. It can only be suggested that the total pressure spikes at the inlet are non-physical and that the data downstream may also have some non-physical influences.

Distortion amplification can be an HCF issue in downstream blade-rows if blade resonance frequencies are low. In general, however, the lowest resonance frequencies can be found in the first rotor. Experimental ADLARF data (Table 3-1) show that some higher frequency distortion components can also propagate through the compressor, in addition to the 3/rev component. Note that the composite distortion amplitude listed in the table is formed from the superposition of the first 24 harmonics with their corresponding phasing.

Table 3-1. Normalized, annulus-averaged amplitude of the significant frequency components of the total pressure distortion measured at various stages in the ADLARF compressor.

Frequency Component	Compressor Inlet Amplitude	Stator 1 Leading Edge Amplitude	Stator 2 Leading Edge Amplitude	Compressor Exit Amplitude
1/rev	.13	.15	.15	.1
2/rev	.06	.11	.12	.1
3/rev	.7	.93	1.4	.9
6/rev	.05	.08	.1	.07
9/rev	.14	.14	.12	.05
15/rev	.08	.05	.06	.03
18/rev	.08	.02	.03	.02
Composite	.98	1.1	1.5	.99

The 2/, 3/, and 6/rev components show a doubling of their amplitudes between the compressor inlet and the Stator 2 leading edge. In general, the compressor acts like a low-pass filter with a corner frequency somewhere between 6/ and 9/rev while the first rotor acts like a low-pass filter with a corner frequency between 9/ and 15/rev. The second rotor is also assumed to act as a low-pass filter; however, the corner frequency must be greater than 15/rev since no attenuation is seen in the major frequency components listed in Table 3-1.

A consequence of the propagating total pressure distortion is the creation of static pressure non-uniformities at the rotor exits. Experimental data for Rotors 1 and 2 are shown in Figures 3-8 and 3-9 while results from the RANS rotor computation are shown in Figure 3-10. These static pressure distortions result from the fact that, despite the presence of the total pressure distortion, the compressor must intake from and exhaust to uniform static pressure fields.

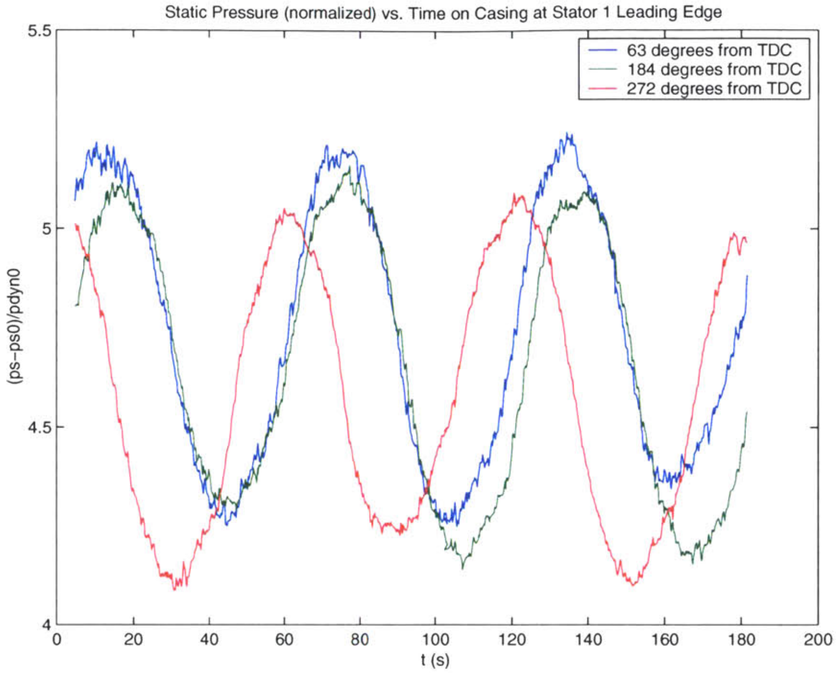

Figure 3-8. Static pressure relative to the upstream average static pressure normalized by the upstream dynamic pressure as measured on the outside casing at the Stator 1 leading edge at three different circumferential locations with respect to top dead center (TDC).

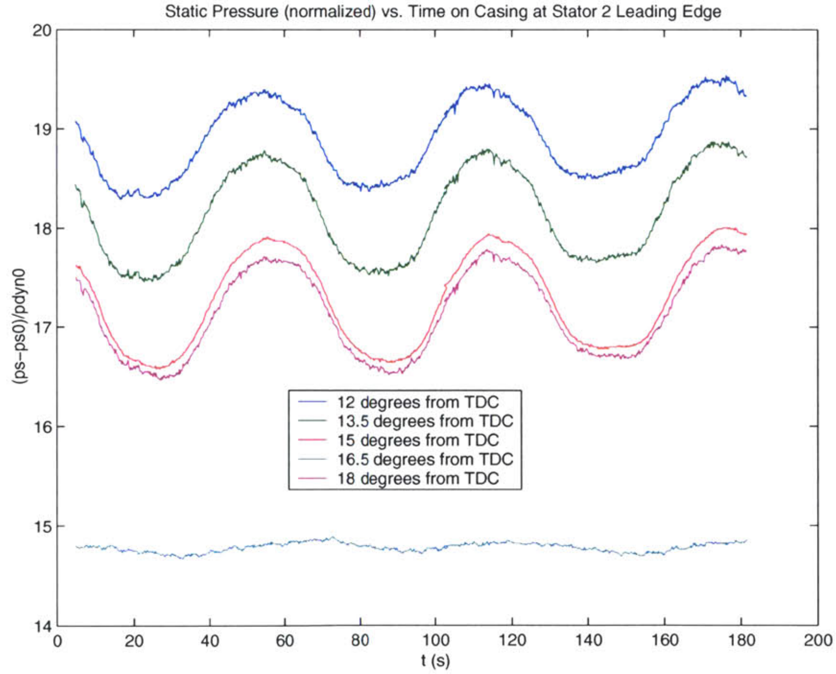

Figure 3-9. Static pressure relative to the upstream average static pressure normalized by the upstream dynamic pressure as measured on the outside casing at the Stator 2 leading edge at five circumferential locations.

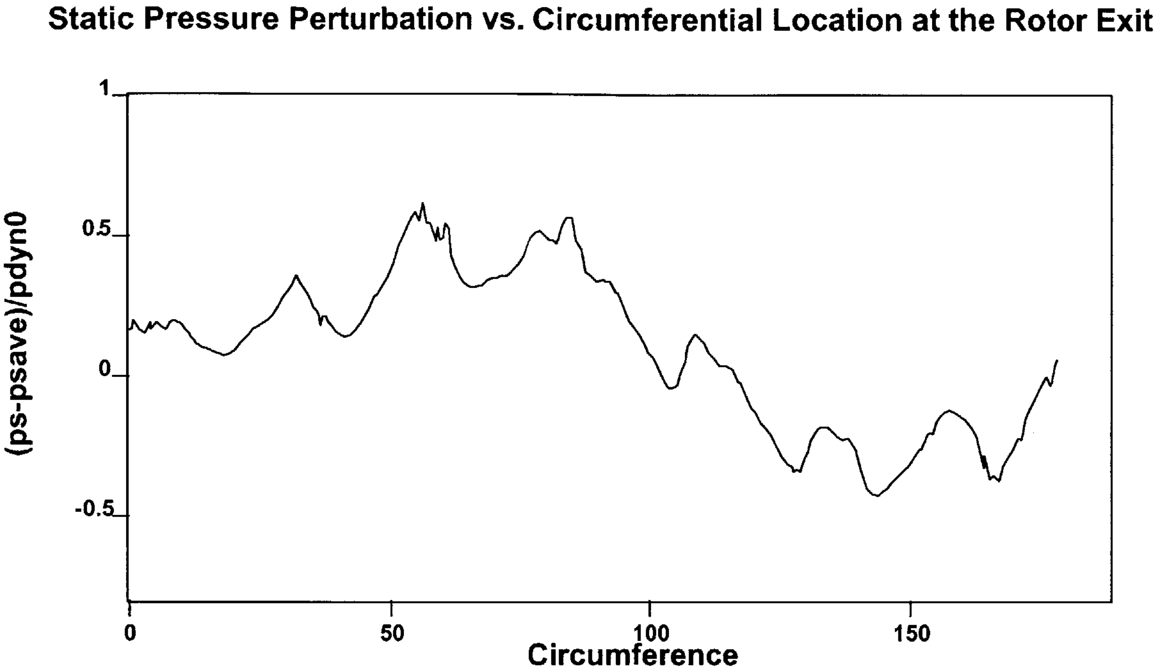

Figure 3-10. Static pressure perturbation normalized by the upstream dynamic pressure at 85% span as computed at the exit of the ADLARF first rotor.

As can be seen in both the experimental and computational data, the amplitudes of the static pressure distortions are of the order of the upstream dynamic pressure. While the experimental data is plotted in the time domain, the fluctuation reflects the circumferential disturbance because the distortion screen is slowly rotating. Note that the pressure tap at 16.5 degrees from TDC appears to have malfunctioned. Offsets in static pressure are seen circumferentially in measurements throughout the compressor. It is unknown whether they are the result of an instrumentation problem or the result of standing acoustic waves in the circumferential direction.

3.3 Distortion Propagation in the Stage 35 Model

In order to corroborate the distortion propagation seen in the ADLARF compressor, a sinusoidal 3/rev total pressure inlet distortion was applied to the NASA Stage 35 compressor model at 72% of its design speed. This model is used below to examine distortion amplification, the distortion of static pressure, and swirl, which is not measured in the ADLARF tests.

The effect of the Stage 35 model on the total pressure distortion is shown in Figure 3-11. Like the ADLARF compressor, Stage 35 also amplifies the distortion. Furthermore, a static pressure distortion is exhibited at the rotor exit (Figure 3-12). As with the ADLARF compressor, the static pressure distortion is also in phase with the total pressure distortion. Thus, the Stage 35 model corroborates the ADLARF distortion amplification and static pressure distortion in a qualitative manner.

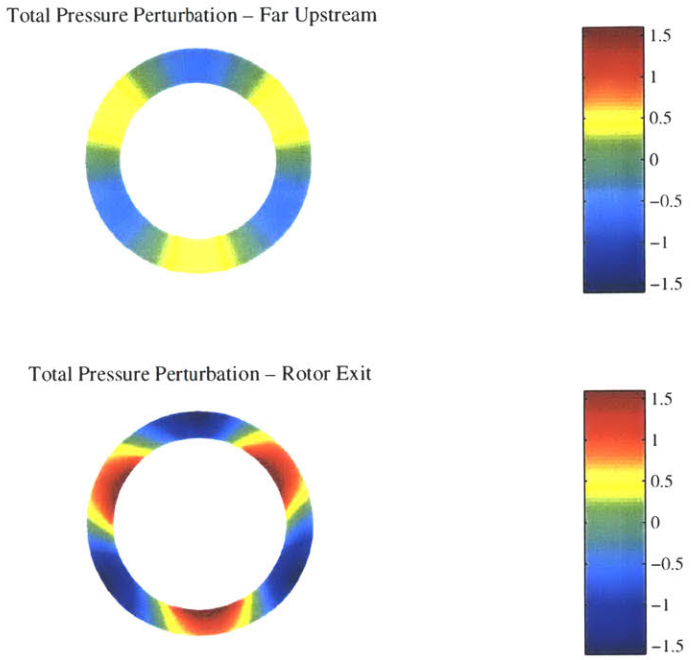

Figure 3-11. Upstream and rotor exit total pressure perturbation normalized by the average bellmouth dynamic pressure.

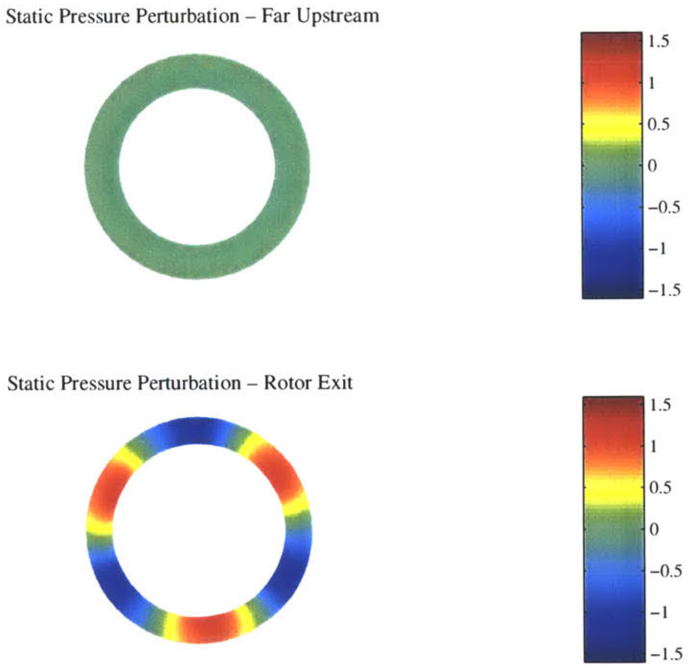

Figure 3-12. Upstream and rotor exit static pressure perturbation normalized by the average bellmouth dynamic pressure.

Another integral feature of an inlet distortion approaching a compressor, especially one without inlet guide vanes, is swirl. Swirl is the response of the flow to the non-uniformity being generated by the compressor in response to the total pressure distortion. Both the static pressure distortion and the resultant swirl begin to develop a short distance upstream of the first rotor where the flow first feels the rotor's presence. That distance falls within one rotor radius of the first rotor face.

Swirl is of interest because it superimposes additional velocity and incident angle non-uniformities on those present due to the total pressure distortion by itself. While the influence of swirl is not addressed by this research, the presence of swirl is reflected in the flow angle distribution at the face of the Stage 35 rotor (Figure 3-13a). As one might expect, the circumferential velocity vectors show flow from regions of high static pressure to regions of low static pressure. Thus, the circumferential velocity is 90° out of phase with the static pressure distortion. Relative flow angle (Figure 3-13b), which is important to blade loading, then has a more complicated pattern—but still 3/rev—because it reflects the superposition of the effects of the total pressure distortion in addition to those from swirl.

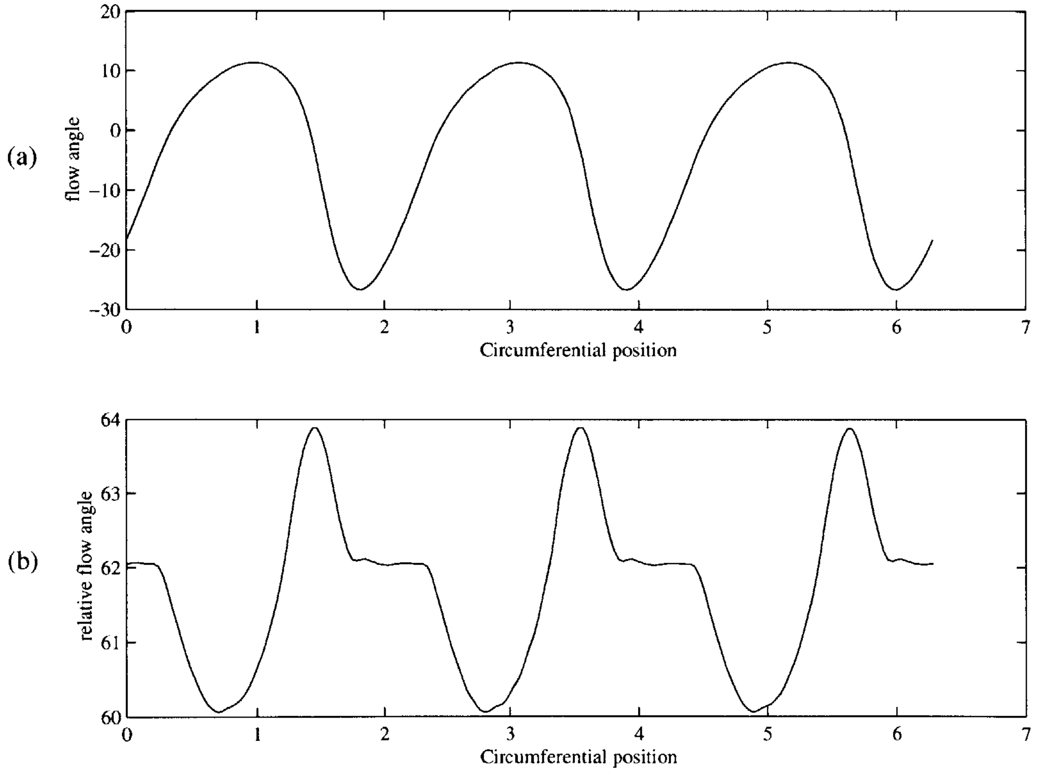

Figure 3-13. (a) Absolute and (b) relative flow angle at mid-annulus at the rotor inlet.

3.4 Discussion

Results were presented regarding distortion amplification, static pressure distortion, filtering characteristics, and swirl in a transonic compressor. Amplification of the 3/rev distortion across the rotors and the presence of static pressure distortions at the rotor exits are seen in both the ADLARF data and the Stage 35 results. ADLARF experimental data also show that the rotors, and the compressor as a whole, act as low-pass filters, allowing only components of the distortion near or below the corner frequencies to pass. Swirl is shown at the rotor face of the Stage 35 model—it is due to the non-uniformity induced by the rotor as it interacts with the total pressure distortion.

Based on the results presented in Sections 3.2 and 3.3, it is clear that, in order for a distortion to propagate through a transonic compressor,

(1) the distortion frequencies must be near or less than the low-pass corner frequency.

(2) the operating conditions should be such that those low frequencies would not be significantly attenuated.

In the case of the inlet distortion in this research, the dominant (3/rev) frequency component is below the corner frequencies of the rotors. Also, the rotors amplify the dominant distortion frequency.

The following two subsections explore the physics that set the filtering and amplification characteristics of a compressor. Static pressure non-uniformities are also discussed, but they are mostly dependent on the amplification of the total pressure distortion.

3.4.1 Low-Pass Corner Frequency

The low-pass corner frequency is approximately the frequency at which the response of a low-pass filter starts to drop off. The corner frequency for any filtering effect is dependent on time (or length) scales. In order to transmit a signal, the transmitting medium must be able to respond at the same rate that the signal magnitude changes. This required response time can be assumed to be of the same order as the signal's period, which is inversely proportional to the signal frequency. Therefore, the higher the frequency is (or the shorter the wavelength is), the shorter the required response time.

The length scale for minimum response time (i.e. corner frequency) can be assumed to be of the same order as the corner frequency wavelength. A length scale commonly used in compressor analysis is chord length. This length scale shows up in a non-dimensional parameter that characterizes the importance of flow unsteadiness: the reduced frequency. The reduced frequency is the ratio of the steady (through-flow) timescale to the unsteady (disturbance) timescale. Alternatively, when divided by 2π, it is the approximate number of distortion cycles, or disturbance wavelengths, along the blade chord at any given time. Reduced frequency is calculated as follows:

$$f_R = \frac{N_d N c_{ax}}{V_{ax}}$$

where N_d is the number of distortion cycles per rotor revolution (or, alternatively, N_d is the EO of the incident frequency), N is the rotation speed of the compressor, c_{ax} is chord length in the axial direction, and V_{ax} is the estimated average axial velocity at the inlet to the first rotor.

The reduced frequency of the first EO at 85% span of the first rotor and 71% operating speed is approximately 1.19, or .19 distortion cycles per chord. The reduced frequency for the ninth EO is then approximately 10.7, or 1.71 distortion cycles per chord. Since the corner frequency for the first rotor occurs between the 9th and 15th EOs, this places the appropriate length scale for corner frequency around one-half blade chord. In other words, if the wavelength of the distortion (in the chord-wise direction) is less then one-half the blade chord, the distortion is likely to be filtered out. For frequencies above the corner frequency set by the half-chord length, the blade responds more to an average of the unsteady pressures. The reason for this is that most (approximately 80%) of the work done by the blade is done in the first half of the chord, which has the largest pressure differences between the pressure and suction surfaces (Figure 3-14).

Figure 3-14 shows the static pressure distribution at 85% span from the RANS rotor compuntation. Note that the pressure differences across the blades are larger than expected—more than twice the upstream dynamic pressure—however, the information regarding distribution of work along the chord is as expected.[1]

The lack of filtering seen by Rotor 2 (Table 3-1) suggests that the corresponding reduced frequencies are lower for Rotor 2 than for Rotor 1. Indeed this is the case as the Rotor 2 chord length is approximately one-third the Rotor 1 chord length. This should put the corner frequency of Rotor 2 up above the 27th EO, which cannot be verified since frequency components above the 18th EO were at the noise level throughout the compressor.

The compressor, as a whole, shows some additional filtering (a lower corner frequency) which must take place between the Stator 2 leading edge and the compressor exit measurement station. It is unclear why additional frequencies are filtered out after Rotor 2 since the total pressure distribution should be quasi-steady (due to the slow rotation of the distortion screen) for stators. However, it is possible that there are some additional losses in this region that lead to increased filtering.

---

[1] This concern has been communicated to Chunill Hah (NASA-GRC), the auther of the numerical code.

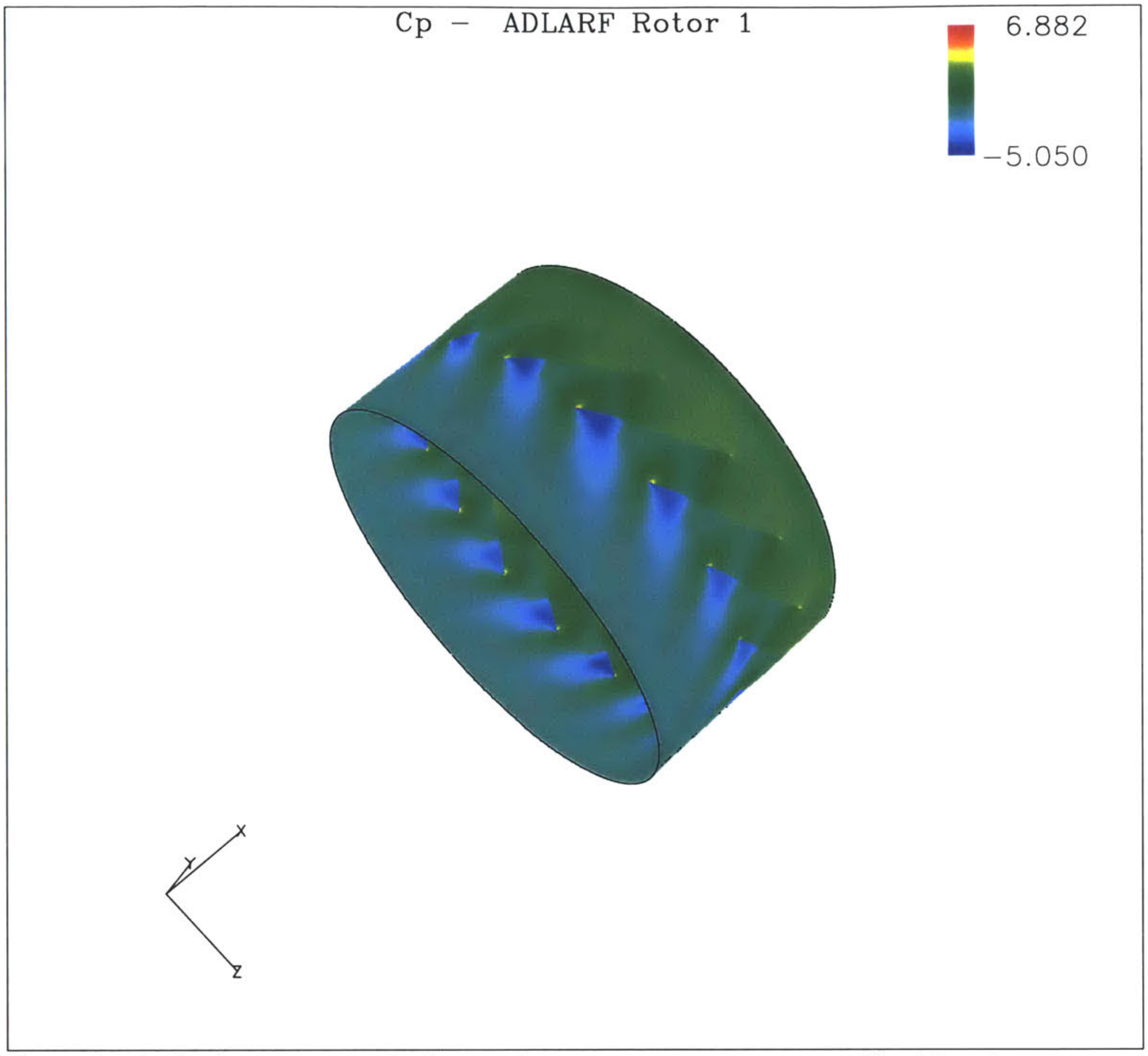

Figure 3-14. Static pressure relative to the average pressure normalized by the upstream dynamic pressure for the ADLARF first rotor at 85% span (NASA calculation).

3.4.2 Distortion Amplification

The objective of this section is to determine if parallel compressor theory [13] can be used to qualitatively explain the observed trends in the data. Appendix D explains how parallel compressor theory uses steady-state pressure ratio curves to predict compressor performance for (unsteady) distorted flow. The two main predictions of parallel compressor theory are compressor performance and distortion amplification. Two important assumptions for parallel compressor theory for high-speed compressors are (1) uniform flow sectors that result in quasi-steady flow through the blades and (2) negligible circumferential flow redistribution. Therefore, the fact that the distortion is sinusoidal and the possibility that there may be swirl at the compressor inlet may both detract from the applicability of parallel compressor theory. Nonetheless, this section compares crude predictions of distortion amplification using parallel compressor theory for high-speed compressors to measurements of distortion amplification in the ADLARF compressor.

It can be inferred from parallel compressor theory that, for the case of a flat pressure ratio curve, the distortion amplification across a compressor or stage is simply the pressure ratio. As is shown by ADLARF data in Chapter 4, the pressure ratio curves for Rotor 1 and for the Stator 1 – Rotor 2 combination are indeed flat. Table 3-2 compares the distortion amplification derived from Table 3-1 with the pressure ratios seen in next chapter's Figure 4-1. Note that the composite distortion referenced in the table is formed from the superposition of the first 24 harmonics with their corresponding phasing.

Table 3-2. Comparison of the experimental distortion amplification factors of the significant frequency components of the total pressure distortion with the parallel compressor theory prediction.

Frequency Component	Rotor 1 Amplification	Stator 1 – Rotor 2 Amplification
1/rev	1.2	1.0
2/rev	1.8	1.1
3/rev	1.3	1.5
6/rev	1.6	1.3
9/rev	1.0	.86
15/rev	.62	1.2
18/rev	.25	1.5
Composite	1.1	1.4
Parallel Compressor	1.6	1.5

For Rotor 1, the amplification of the composite distortion signal falls significantly short of the parallel compressor prediction. This is most likely due to the filtering of high frequency distortion content by Rotor 1, as discussed in Section 3.4.1. It is also evidenced by the better agreement that the lower frequency component amplifications show with the parallel compressor prediction. The results of the RANS calculation of Rotor 1 (Figures 3-6 and 3-7) show an amplification factor of approximately five.

The above analysis shows how to determine the total pressure distortion amplification expected across a compressor or stage that has a flat pressure ratio curve. The relationship between the slope of the pressure ratio curve and total pressure distortion amplification is discussed in more detail in Appendix D.

Also addressed in Appendix D, pressure ratio curves (indirectly) yield information about the static pressure distortions at the rotor and compressor exits. The relationship is more directly seen in looking at total-to-static pressure rise curves, however. The resulting relation is as follows:

$$(p_{2H} - p_{2L}) = (p_{t1H} - p_{t1L})(1 + Cb)$$

where b is the slope of a line drawn between the two performance points and C, which is positive, is the amplitude of the distortion in corrected mass flow rate divided by the amplitude of the total pressure distortion. Comparing the values of the last term in parenthesis, one can see that a very large negative slope will result in a static pressure distortion out of phase with the total pressure distortion. As discussed in Appendix D, a large negative slope also results in the attenuation of the total pressure distortion across the compressor or stage. For most high-speed compressor configurations, the static pressure distortion will be out of phase with the total pressure distortion if the absolute total pressure distortion is attenuated and in phase if the absolute total pressure distortion is amplified. Thus, the static pressure distortion is coupled to compressor performance and care must be taken in setting boundary conditions for calculations.

3.5 Summary of Observations and Deductions

The study of distortion propagation through the ADLARF compressor, the Stage 35 model, and the RANS ADLARF rotor model results in the following observations and deductions:

1. The rotors of the ADLARF compressor amplify the total pressure distortion. Likewise, a similar trend is seen in calculations performed for 3/rev distorted flow through the NASA Stage 35 and RANS ADLARF rotor models.

2. The RANS ADLARF rotor model over-predicts distortion amplification.

3. The experimental ADLARF compressor data, the results from the Stage 35 model, and the results from the RANS rotor computation show static pressure distortions at the rotor exits which are in phase with the total pressure distortion.

4. The ADLARF compressor rotors act as low-pass filters—filtering out the higher distortion frequencies.

5. As to be expected, computed flow for the Stage 35 rotor subjected to a 3/rev inlet distortion indicates swirl local to the distorted sector in response to the resulting static pressure non-uniformity.

6. Filtering corner frequency of the rotors is set by a length scale of approximately one-half chord—shorter wavelengths are filtered by the rotors.

7. Parallel compressor theory qualitatively predicts distortion amplification for the ADLARF compressor.

8. Single rotor calculations need to take into account the static pressure distortions that result from total pressure distortions if the outflow boundary condition is not located sufficiently far downstream.

Chapter 4

COMPRESSOR PERFORMANCE

This chapter focuses on ADLARF total pressure and total temperature rake data at various axial locations in the flow path of the compressor. The objective is to determine the inlet distortion's effect on compressor performance. Results are presented in the form of pressure ratio, efficiency, and temperature ratio versus corrected mass flow rate. Performance values from the ADLARF first rotor RANS computation are provided for comparison. Results are then interpreted and discussed in terms of the resulting changes in performance and stall margin.

4.1 ADLARF Experimental Results

The impact of the 3/rev total pressure distortion on ADLARF compressor and stage pressure ratios is shown in Figure 4-1, which compares four operating points along the 71% speed line for distorted and clean inlet conditions. Because total pressure and temperature measurements were taken at the leading edges of the stators, results are presented for Rotor 1 by itself, the Stator 1 – Rotor 2 combination, and the entire compressor, which includes the aforementioned in addition to Stator 2.

From left to right, the operating points are NS, PE, NOL, and WOD. The NS and PE conditions were determined during testing, while NOL was set by the compressor design and WOD was set by the facility. As can be seen, under the 3/rev distortion, the change in performance is minimal although the measured range of operability has shifted. Note that the curves for Rotor 1 and for the Stator 1 – Rotor 2 combination are relatively flat while the curve for the entire compressor drops off with increasing mass flow rate. This drop-off is due to increasing losses over the last row of stators as the mass flow rate increases.

The efficiency curves for the entire compressor and for Rotor 1 (Figures 4-2 and 4-3) also show little change in performance despite the shift in operability range. The efficiency curve for the Stator 1 – Rotor 2 combination (Figure 4-4), however, shows degradation in performance in addition to the shift in operability range. There is a significant drop in efficiency for the NS, PE, and NOL operating points. Figure 4-5 shows that the temperature ratios for these operating points are higher for the distorted flow.

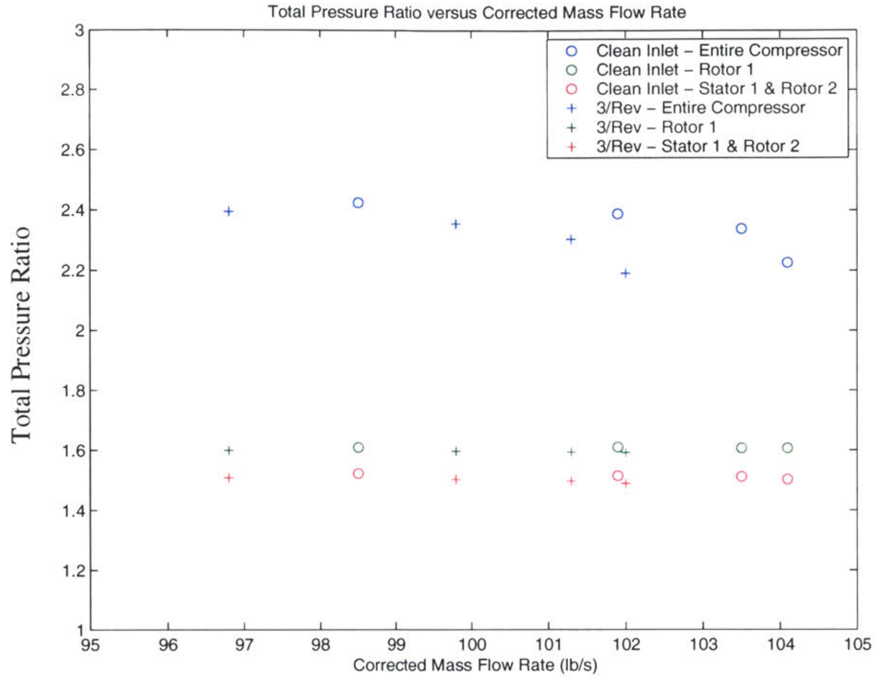

Figure 4-1. Total pressure ratio versus corrected mass flow rate for the entire compressor, for Rotor 1, and for the Stator 1 – Rotor 2 combination when subjected to clean and distorted inlet flow.

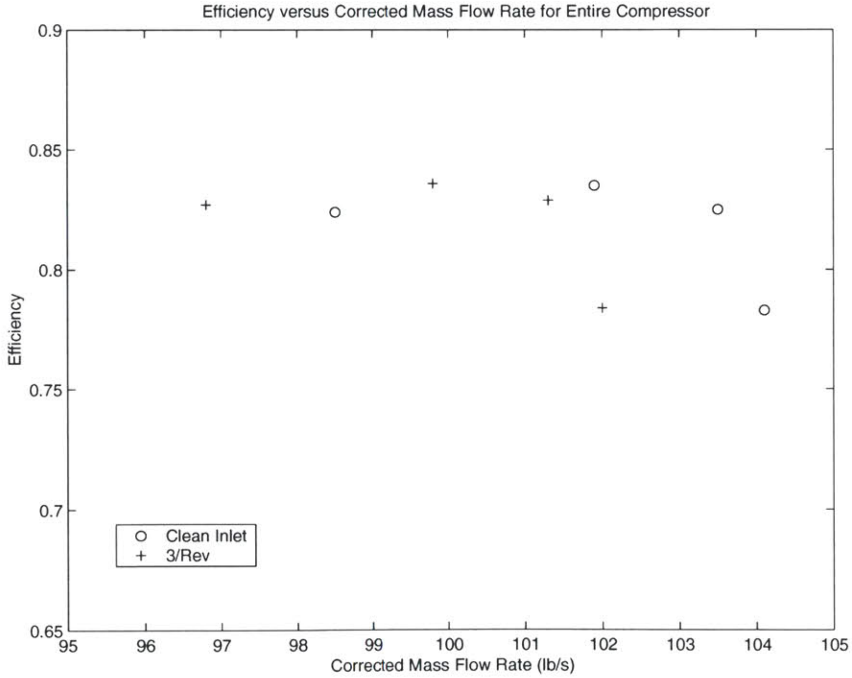

Figure 4-2. Efficiency versus corrected mass flow rate for the entire compressor for clean and distorted inlet flow.

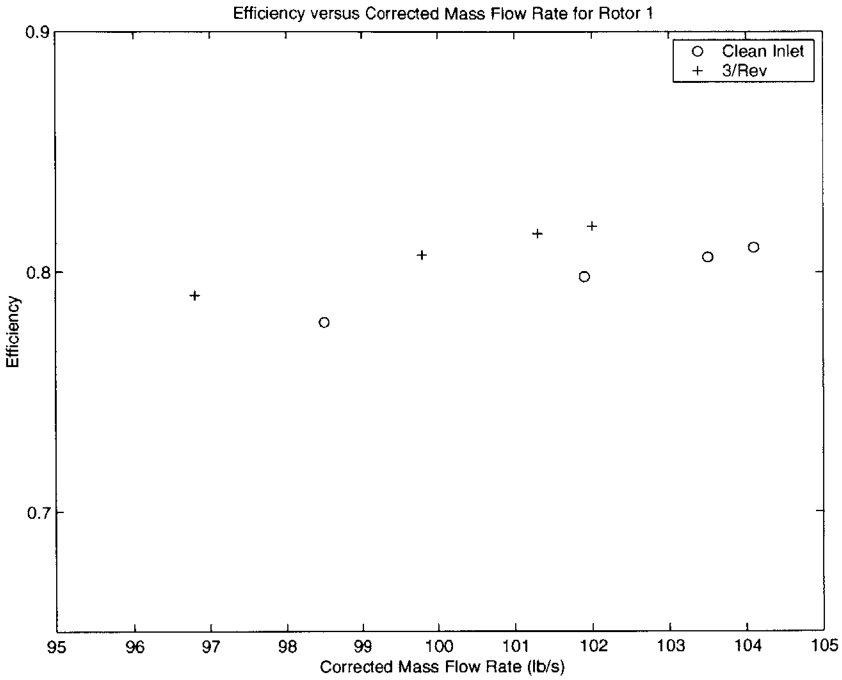

Figure 4-3. Efficiency versus corrected mass flow rate for Rotor 1 when subjected to clean and distorted inlet flow.

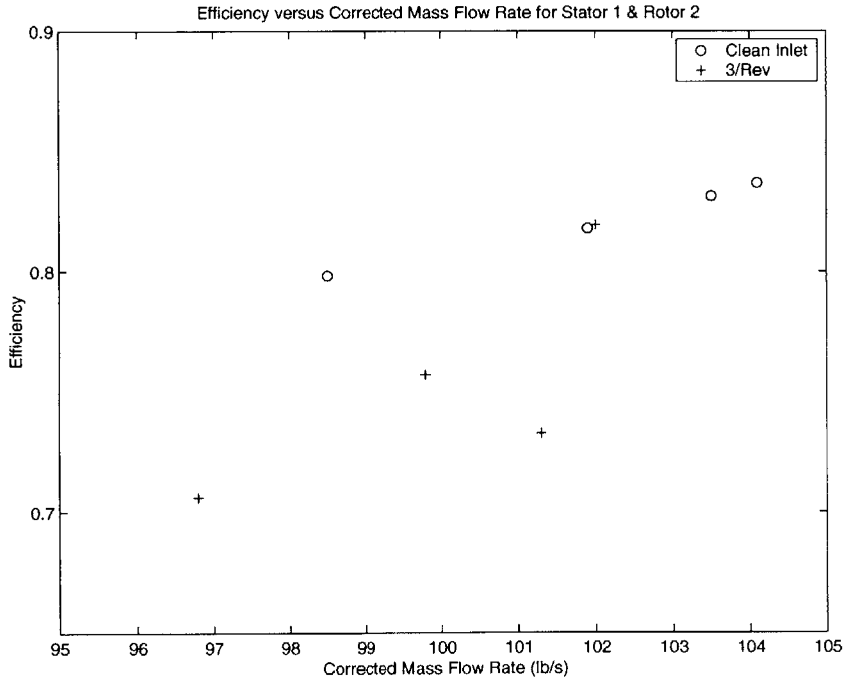

Figure 4-4. Efficiency versus corrected mass flow rate for the Stator 1 – Rotor 2 combination when subjected to clean and distorted inlet flow.

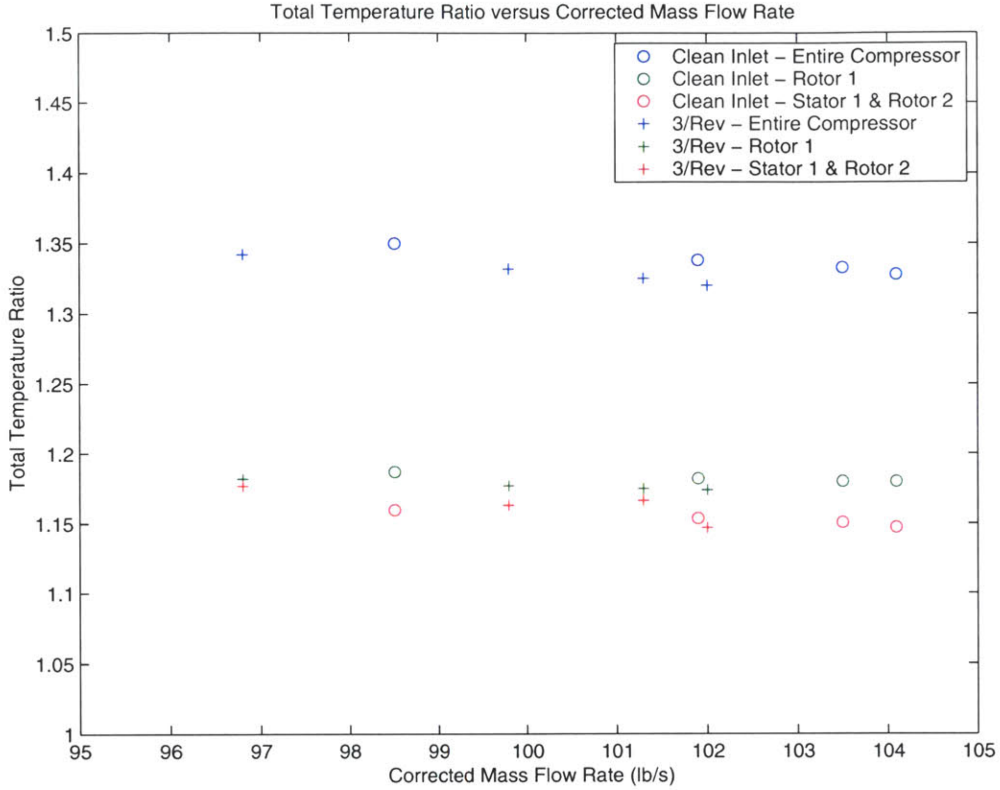

Figure 4-5. Total temperature ratio versus corrected mass flow rate for the entire compressor, for Rotor 1, and for the Stator 1 – Rotor 2 combination when subjected to clean and distorted inlet flow.

4.2 Results from the RANS Computation of the ADLARF First Rotor

The ADLARF first rotor computation was carried out on the 71% speed line near the PE operating point. For this reason, experimental values at the distorted PE operating point are used for comparison with the computational results.

The pressure ratio for the RANS first rotor computation is 1.58, which is approximately 1% lower than the distorted PE operating point. The temperature ratio for the first rotor computation is 1.16, which is approximately 2% lower than the distorted PE operating point. Although these differences in temperature and pressure ratio are small, the resulting difference in efficiency is not. The efficiency for the RANS first rotor computation is .873, which is approximately 9% higher than the distorted NS operating point.

4.3 Discussion

Based on the experimental results, the general impact of the 3/rev distortion on ADLARF compressor and stage performance was marginal despite a shift in the operability range.

The efficiency curve of the Stator 1 – Rotor 2 combination was the only curve to show degradation in performance.

The lack of significant change in performance despite the presence of the inlet distortion is an interesting feature because, in many situations involving distorted flow, there are significant degradations in both pressure ratio and efficiency. This deviation from the norm may be due to the unsteadiness of the flow. One might speculate that flow that would normally stall blades under steady-state conditions might be too short-lived to result in any appreciable losses, let alone stall. High-speed flow segments that would have significant losses under steady-state conditions might also be too short-lived to result in the boundary layer growth that results in significant losses.

Recall from Section 3.4.1 that reduced frequency offers a measure of a flow's unsteadiness. A reduced frequency near one implies that both quasi-steady and unsteady effects influence the flow field around the rotor blades while a reduced frequency much greater than one implies that unsteady effects dominate [14]. The 3/rev distortion in the ADLARF tests falls more towards the unsteady category—it has a reduced frequency of approximately 5.83 at the 85% span of the first rotor when operating at 71% design speed. Thus, loss mechanisms relating to stall or high velocity might not have time to establish themselves.

The shift of the NS point along with the other operating points represents an improvement in stall margin when the ADLARF compressor is subjected to the 3/rev inlet distortion. This is an interesting feature because inlet distortions can often reduce a compressor's stall margin. However, one can conjecture that the same unsteadiness that may mitigate losses at the other operating points delays the onset of stall as reflected in the NS point. It can then be inferred that, in the region of improved stall margin, the reduced frequency is high enough (presumably greater than one) and the high-speed flow segments are fast enough (presumably within the clean flow operability range) to prevent the full development of stall. Therefore, one might hypothesize that distortion amplitude as well as reduced frequency plays a role in compressor performance under inlet distortion.

Results from the RANS rotor computation show that it predicts average distorted pressure and temperature ratios to within one or two percent of the experimental values. As shown, however, these small deviations result in an over-prediction of the first rotor's efficiency by approximately nine percent. Clean flow computations were not analyzed. Therefore, it is unknown whether this discrepancy in performance would be present for clean flow, as well. Another possibility for discrepancy is, of course, measurement uncertainty.

4.4 Summary of Observations and Deductions

In studying the effect of the 3/rev inlet distortion on ADLARF compressor performance, the following observations and deductions have been made:

1. The distortion caused minimal change in total pressure and temperature ratios despite a shift in the operability range.

2. The stall margin improved under distorted flow.

3. The unsteadiness of the distorted flow may be responsible for both minimizing losses and improving stall margin in the distorted flow—reduced frequency and distortion amplitude may be important parameters for compressor performance under sinusoidal total pressure distortions.

4. The ADLARF RANS rotor model predicts pressure and temperature ratio for distorted flow to within one or two percent. The resulting efficiency, however, is over-predicted by nine percent.

Chapter 5

BLADE AERODYNAMICS AND STRUCTURAL RESPONSE

This chapter examines ADLARF experimental data on the blade and experimental and computational data in the blade passage. The objective is to determine distortion induced blade passage events and the resulting force and response scenario. First, LDV and computational data in the blade passage are examined to identify the flow field and any distortion induced events. Second, on-blade kulite and strain gauge data are presented and analyzed in terms of force, response, and vibration modes. Finally, the results are summarized and discussed.

5.1 Flow Characterization

Figures 5-1 and 5-2 show LDV measurements [1,4] of a blade passage at 85% span subjected to the high- and low-speed segments of a 3/rev distortion. The high-speed segment of the distortion corresponds to the region of high total pressure while the low-speed segment corresponds to the region of low total pressure (Figure 3-5). The measurements are at 62% design speed, which should show lower Mach numbers than those expected for 71% design speed—the speed on which the analysis of this thesis focuses. Computational results for distorted flow at 85% span (Figure 5-3) are at 71% design speed but are based on a smaller total pressure distortion (Figure 3-6) than the experimental data indicate (Figure 3-5).

Both LDV figures show evidence of a compression at the suction-side leading edge. Comparing the figures, it can be seen that there are fluctuations in Mach number, which are to be expected, and that the fluctuation of the transonic flow region near the suction-side leading edge is at 3/rev, as expected. Two interesting features that do not appear in clean flow are the high Mach number prong stretching aft along and just offset from the pressure surface and a pitch-wise strip of lower Mach number flow that gets swallowed up and reappears as the distortion cycles. The high Mach number prong may be caused by vortex shedding or flow blockage due to separated flow at the suction side leading edge, or it may simply be the result of blade overloading, as the blade and its solidity are designed for a certain flow angle and flow rate. The pitch-wise, low-speed strip may be the result of a weak travelling pressure wave resulting from the motion of the leading edge transonic region.

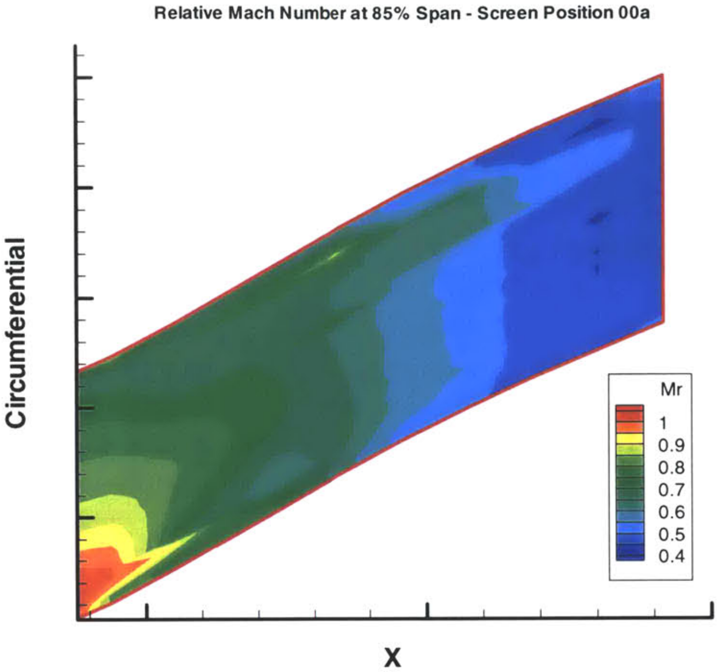

Figure 5-1. LDV measurements of relative Mach number in the blade passage at 85% span subject to the high-speed section of a 3/rev distortion at 62% design speed.

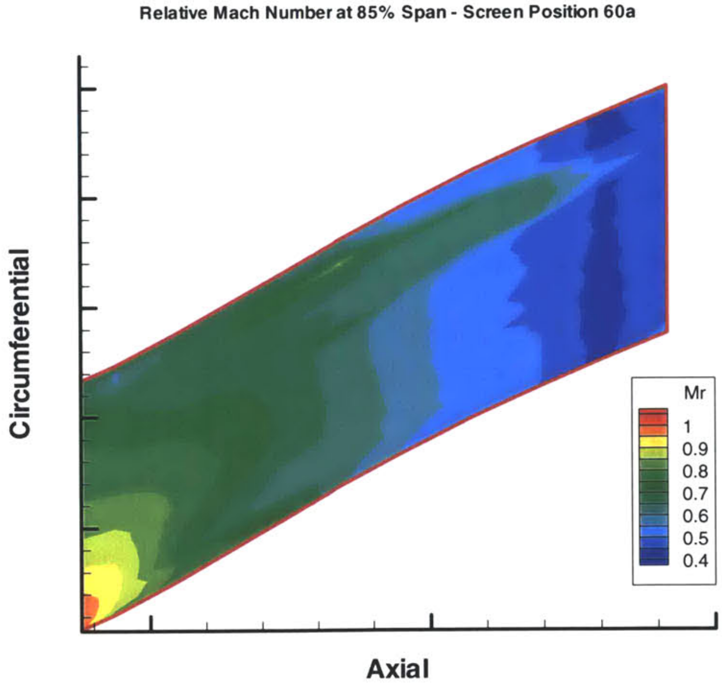

Figure 5-2. LDV measurements of relative Mach number in the blade passage at 85% span subject to the low-speed section of a 3/rev distortion at 62% design speed.

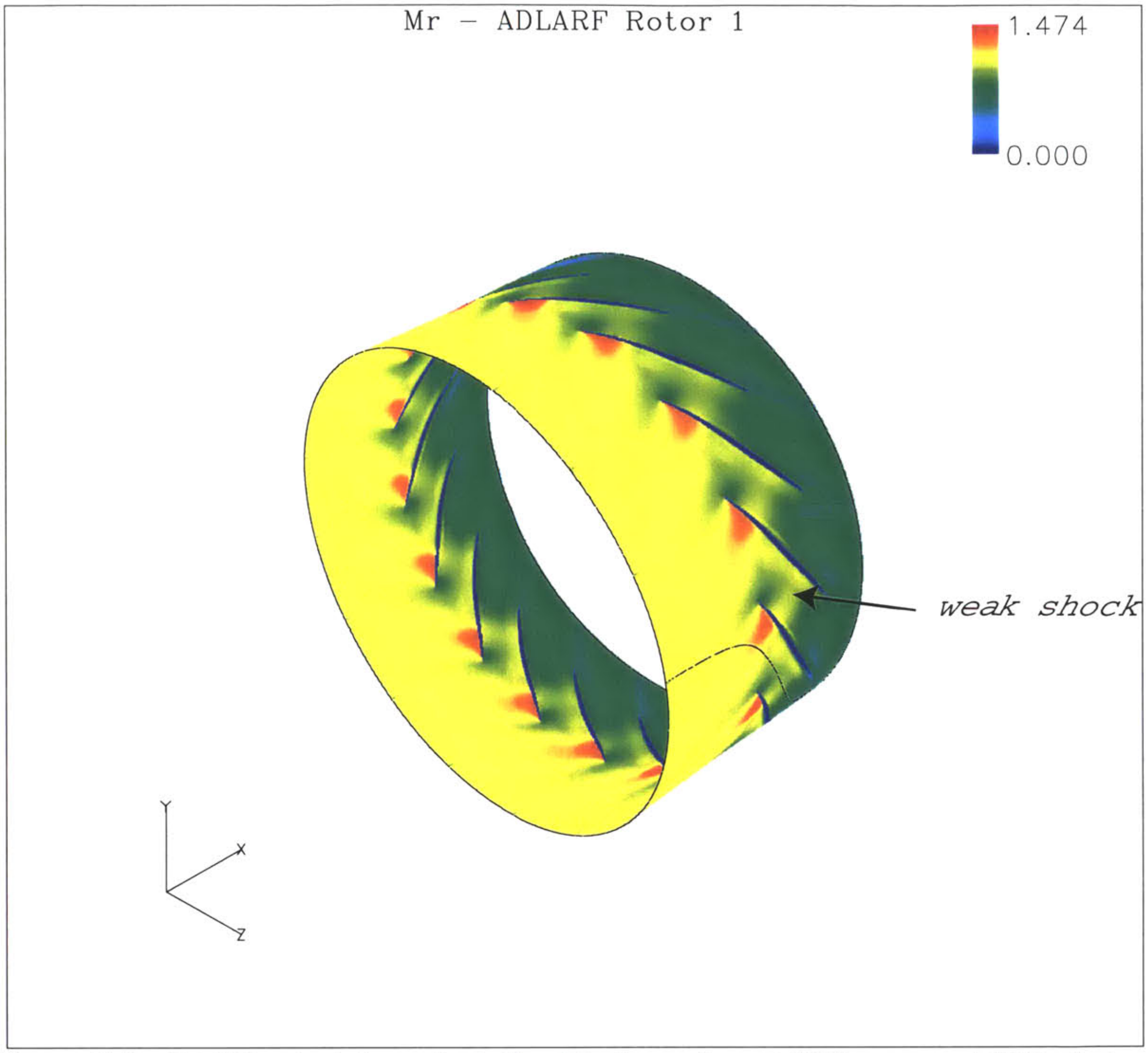

Figure 5-3. RANS calculation of relative Mach number at 85% span and 71% design speed for distorted flow through the ADLARF first rotor.

The computational data show supersonic regions near the suction-side leading edges followed by mostly subsonic flow through the blade passages. There is evidence of a weak shock in a few of the blade passages—its presence appears to be associated with blades that have the largest supersonic regions. Associated with the blades that have smaller supersonic regions are larger blade wakes. The transient computational data show the appearance and dissappearance of the weak shock and the growth and reduction in the extent of the wakes, both at the distortion frequency. As can be inferred in the next section, flow events such as these can not be identified from the on-blade ADLARF kulite data.

5.2 ADLARF Blade Data

5.2.1 Kulite Data

Differential pressure data consist of kulites mounted along the 85% span on two adjacent blades. Differences in amplitude and phase occur from sensor to sensor as shown in Figures 5-4 and 5-5, which focus on the 3/rev frequency component of differential pressure for both clean and distorted flow. Note that Blade 1 is missing measurements from the second kulite from the leading edge.

Clean flow shows approximately constant differential pressure amplitude and an approximately linear progression in phase on both blades. This linear progression of phase reflects an almost constant signal convection velocity along the 85% span, with the convection speed along Blade 1 being slightly higher than that of Blade 2.

The amplitude and phase of the 3/rev component in the distorted flow show significant variation in the first third of the Blade 2 chord. The second kulite shows an amplitude four times higher than the amplitudes of the other kulites. Keeping in mind the periodicity of phasing, the progression of phase along the first four kulites shows a low (phase) convection speed between Kulites 1 and 2 and an increasing convection speed in the chord-wise direction until a constant convection speed is achieved after the fourth kulite. Separation could be responsible for the slow convection speed of the 3/rev phase in the first third of the chord, but it would not likely be responsible for the high amplitude unless the flow were only temporarily separated. Thus, the slow convection speed and increased 3/rev amplitude in the first third of the blade chord may indicate that flow is separating and re-attaching to the blade in response to the distortion.

5.2.2 Blade Force

A blade force was calculated from each set of kulites. Kulite 2 on Blade 2 was left out of calculations—except where noted—for more appropriate blade-to-blade comparisons. The calculated blade force is meant to be representative of the forcing function exerting a bending moment on the blade. It is important to note that, the blade force is really the result of the forcing function as well as forces due to aerodynamic damping, as the flow may resist or assist the motion of the blade. Therefore, using this experimentally derived force as the forcing function in a force and response analysis may be inaccurate if aerodynamic damping is large or if the span-wise measurements are a poor representation of the total bending force.

Blade force frequency content for the two adjacent blades is shown in Figure 5-6. Neither blade showed any significant frequency content above the 6/rev component, so force amplitudes are only shown for the first six EOs. The frequency content of blade forces calculated from clean inlet data is provided for comparison.

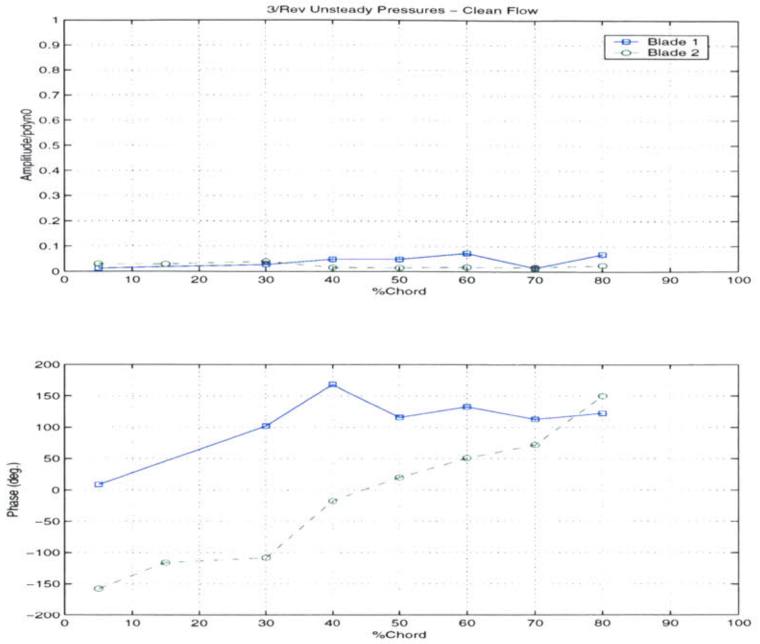

Figure 5-4. The 3/rev phase and the 3/rev differential pressure amplitude normalized by the dynamic pressure at the bellmouth versus chord for two adjacent blades in clean inlet flow.

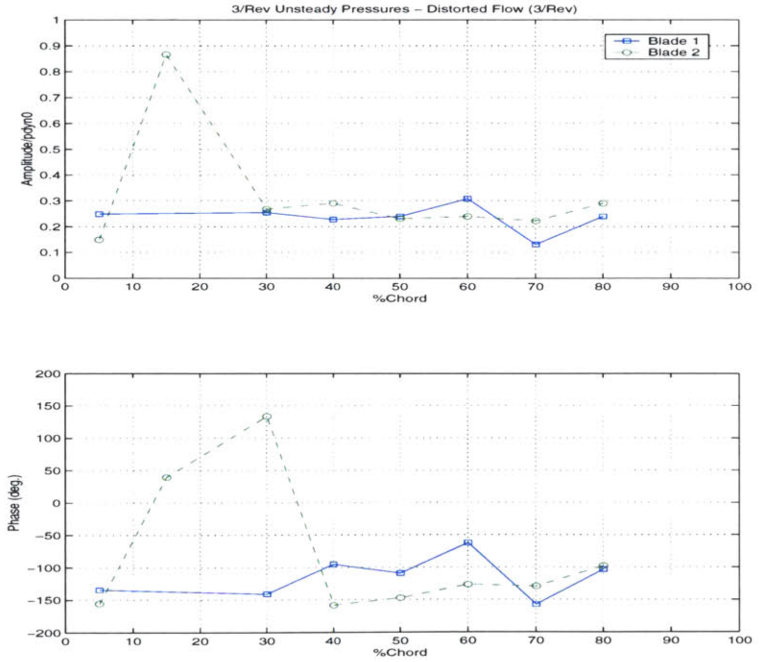

Figure 5-5. The 3/rev phase and the 3/rev differential pressure amplitude normalized by the dynamic pressure at the bellmouth versus chord for two adjacent blades in distorted flow.

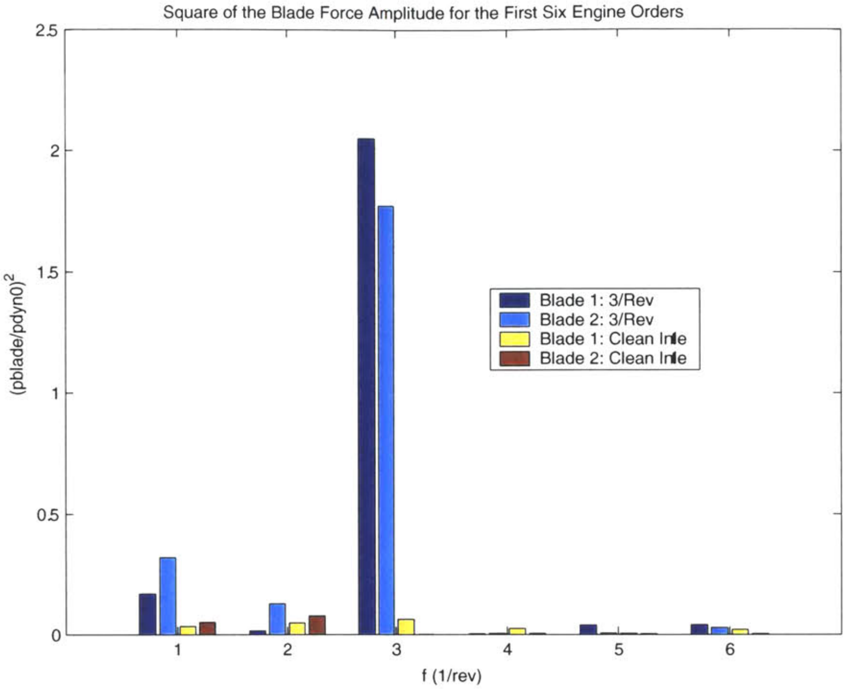

Figure 5-6. Blade force power spectral density for two adjacent blades under the influences of a 3/rev distortion and clean inlet flow.

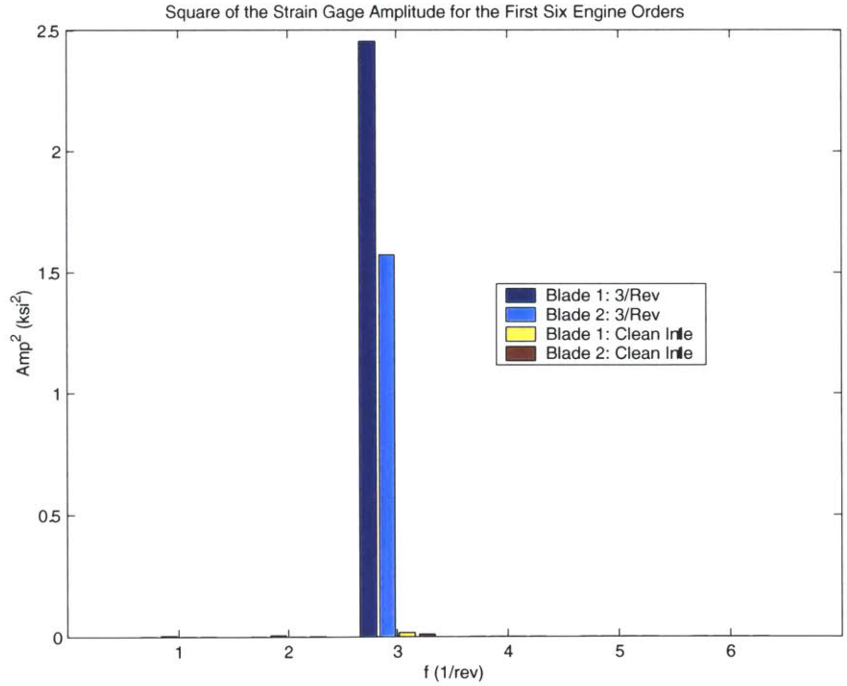

Figure 5-7. Blade strain power spectral density for two adjacent blades under the influences of a 3/rev distortion and clean inlet flow.

The 1/ and 3/rev frequency components for the blade forces in the distorted flow are present due to the inlet distortion. (See values under the heading "Compressor Inlet Amplitude" in Table 3-1.) The rest of the frequency components are of unknown origin, with the possible exception of the 3/rev component of force for Blade 1 in clean flow. This component may be due to small 3/rev blade motions resulting from the proximity of the third EO to the 1F resonance frequency.

5.2.3 Blade Strain (Response)

Strain gauge data consist of base-mounted strain gauges on five adjacent blades (including the kulite-mounted blades) and leading and trailing edge strain gauges on four adjacent blades (also including the kulite-mounted blades). The frequency content of the base-mounted strain gauges is shown in Figure 5-7 for the two kulite-mounted blades. Again, frequency content from clean inlet data is provided for comparison.

The response of the blades in both clean and distorted flow is almost exclusively 3/rev. The reasons for this are:

(1) the proximity of the third EO to the 1F resonance frequency

(2) the ideal location of base-mounted strain gauges for picking up the 1F mode

The measurements from a handful of leading and trailing edge strain gauges were also analyzed. They showed small but significant 8/ and 12/rev components in addition to the dominant 3/rev component. The presence of the 8/ and 12/rev components indicate that those strain gauges are located where bending would occur for some of the corresponding blade modes—2F-1T and 2S. Since the kulites show no trends with respect to the 8/ and 12/rev frequencies, it must be assumed that the drivers to these excitations are not occurring at the 85% span, in the chord-wise direction.

5.2.4 Blade-to-Blade Phase Comparisons

Since the base-mounted strain gauges only responded to the 3/rev force component, the force and response data were characterized for their 3/rev frequency content only. Table 5-1 compares blade force and strain phasing between the two adjacent blades. Values from the clean inlet data are also provided for comparison.

Table 5-1. Distorted and clean inlet phase comparisons between Blades 1 and 2 (ϕ_{b1}-ϕ_{b2}) for the 3/rev components of blade force and base strain.

Comparison of Blades 1 & 2	3/Rev Distortion	Clean Inlet
Blade Force Phase Difference	-331°	-76°
Blade Strain Phase Difference	-70°	-28°

The phase difference between the adjacent strain data for the distorted flow is close to the –67.5° phase difference expected of a 3/rev backward traveling wave on a 16-blade rotor. This is seen between all five instrumented blades. The blades are moving at the interblade phase angle despite the fact that the phasing of the forces (at least on two blades) is far from the interblade phase angle. This may indicate that there is blade-to-blade coupling through blade passage aerodynamics or structurally through the blisk, enabling the 16-blade system to oscillate at its fourth-mode natural frequency. It is difficult, however, to explain the phase difference between the blade forces since pressures were only measured on two adjacent blades. Cascade effects, blade passage events, inadequate measurement of blade force, and the presence of significant aerodynamic damping forces could all play a role in disrupting the 3/rev blade force phase measurements.

For the clean inlet case, the phase differences between the five adjacent base strains vary significantly, indicating that the effects are not significant enough to cause oscillation of the cascade as a sixteen-blade system. This seems plausible since the 3/rev forces on the blade are at the noise level. The phasing between the adjacent blade forces should be random, as well.

5.2.5 Force and Response Comparisons

A ratio of blade response to blade force can be obtained by dividing the 3/rev blade strain amplitude (Section 5.2.3) by the 3/rev differential blade pressure amplitude (Section 5.2.2). The resulting response-to-force ratios for both clean and distorted flow are shown in Table 5-2.

Table 5-2. Ratio of the 3/rev frequency components of response (strain, in ksi) to those of force (in upstream dynamic pressures) for two adjacent blades subjected to a 3/rev distortion and clean inlet flow.

Blade	3/Rev Distortion	Clean Inlet
1	7.39	3.55
2	7.14	12.2
2*	22.0	18.7

*Measurements from Kulite 2 included in the calculations.

Comparing calculations for Blades 1 and 2 that do not include Kulite 2, one can see that there is a large difference between the Blade 1 and 2 response-to-force ratios for clean inlet flow. This may indicate that the blades are experiencing different amounts of damping. In the case of the distorted flow, the blades appear to be experiencing similar amounts of damping (be it aerodynamic or structural)—evidence that blade coupling through a 16-blade oscillation mode is plausible.

Comparisons between clean and distorted calculations of response-to-force ratio for Blade 2 with Kulite 2 included are closer than clean and distorted comparisons for Blades 1 and 2 without the Kulite 2 measurements. This represents a more linear relationship between force and response, which is what is expected. Therfore, it may also indicate that the measurements from Kulite 2 are vital to adequate calculation of blade force in the span-wise instrumentation configuration.

Phase differences between force and response (strain) are shown in Table 5-3 for both clean and distorted flow. Note that a sign convention relating positive strain to bending in the forward direction was assumed based on the results. No documentation or resident knowledge within the CRF could be discovered, confirming or denying this assumption. A reversal of this assumption would add 180° to each phase difference.

Table 5-3. Phase differences (θ_F-θ_R) between the 3/rev force and response components for two adjacent blades subjected to a 3/rev distortion and clean inlet flow.

Blade	3/Rev Distortion	Clean Inlet
1	-2°	15°
2	-101°	63°
2*	-121°	100°

*Measurements from Kulite 2 included in the calculations.

Assuming each blade to be part of a second-order, linear system, phase differences between force and response should be in the second quadrant for positive damping and in the third quadrant for negative damping. This is due to the fact that the third EO at the operating speed is above the 1F resonance frequency. Both phase differences for Blade 2 with Kulite 2 included are within the two expected quadrants while three out of the four phase differences calculated without Kulite 2 measurements are outside the expected quadrants. This may indicate that the measurements from Kulite 2 are necessary to adequately capture the phase of the blade force in the span-wise instrumentation configuration.

5.3 Summary and Discussion

Experimental on-blade as well as experimental and computational blade passage data were presented to provide some insight into the blade passage events connected with the forced response of compressor rotor blades near their 1F resonance frequency.

Both the experimental (LDV) and computational blade passage data show that the blade passage flow field fluctuates in response to the distorted flow. However, neither the LDV data set nor the computational data set is a perfect match for the ADLARF rake and blade data. The LDV data are at a lower compressor speed than the rest of the experimental data in this thesis, and the first rotor computation uses a smaller amplitude total pressure distortion (Figure 3-6) than is reflected in the experimental data (Figure 3-5).

Kulite data from the 85% blade span show significant variation along the first third of the chord on Blade 2—specifically larger amplitudes and larger changes in the phase of the 3/rev frequency component. Both of these features may indicate separated flow or fluctuation between separated and attached flow. The computational data in Section 5.1 does not indicate separation; however, the computation uses a smaller distortion amplitude than is seen in the experimental data. Kulite 2 on Blade 1 did not provide useable data, so it is unknown whether Blade 1 would also have shown similar variation.

The blade forces calculated from kulite measurements in the distorted flow show a dominant 3/rev component as well as a small but significant 1/rev component; both are due to the frequency content of the original inlet distortion. The blade responses, as measured by the base mounted strain gauges, were almost exclusively at the 3/rev frequency and were significant in magnitude.

Blade-to-blade phase differences in blade force and blade response (strain) indicate that, in the distorted flow, the blades are oscillating near the interblade phase angle for a 3/rev backward travelling wave. The blade forces, however, are not at the interblade phase angle, which may indicate that the blades are oscillating as a 16-blade system, coupled through blade passage aerodynamics or coupled structurally through the blisk. Reasons for the blade force phasing may include cascade effects, blade passage events, inadequate blade force representation, and the presence of significant aerodynamic damping forces.

Results of the force and response analysis are somewhat inconclusive since only two blades were instrumented with both kulites and strain gauges. Since Kulite 2 did not provide useable data on Blade 1, response-to-force ratio and phasing between force and response were presented for Blades 1 and 2 without Kulite 2 measurements and for Blade 2 including measurements from Kulite 2. Blade-to-blade comparisons of response-to-force ratios (without Kulite 2) for clean and distorted flow offer supporting evidence that the blades are oscillating as a 16-blade system in the distorted flow case. Clean and distorted flow calculations for Blade 2 with Kulite 2 included indicate that Kulite 2 improves the accuracy of blade force representation. Still, a computational analysis is necessary to determine if the current measurements (with Kulite 2 included) adequately capture blade force and to determine new measurement locations if blade force is not being adequately captured.

Chapter 6

SUMMARY AND CONCLUSIONS

Experimental data from the ADLARF compressor, results from the NASA high-speed Stage 35 model, and results from the RANS computation of the ADLARF first rotor were used to examine the effect of a 3/rev sinusoidal total pressure distortion on a transonic compressor. Conclusions are presented regarding distortion propagation, compressor performance, blade passage events, experimental issues, and future work.

6.1 Summary

6.1.1 Distortion Propagation

Data from the high-speed two-stage ADLARF compressor, computations of the high-speed NASA Stage 35, and the RANS computation of the ADLARF first rotor show amplification of the 3/rev inlet distortion. Distortion amplification predicted by the RANS ADLARF rotor computation is approximately four times greater than that seen in the ADLARF experimental data. Predictions based on parallel compressor theory, however, are found to be more consistent with the experimental data.

Despite amplifying the distortion, the ADLARF compressor rotors are found to act as low-pass filters. The low-pass corner frequencies are between 9/ and 15/rev for the first rotor and between 6/ and 9/rev for the entire compressor. The Rotor 1 corner frequency is equivalent to a reduced frequency of the order 4π, or 2 distortion cycles per blade chord. This indicates that one-half chord is the filtering length-scale and, hence, the proportion of the blade chord doing most of the work on the flow.

The Stage 35 computational results, the RANS ADLARF rotor computation, and the ADLARF experimental data show significant static pressure non-uniformities at the rotor exits. The phasing and the magnitude of the static pressure distortions are dependent on compressor flow path configuration, downstream components, and the slope of the pressure ratio curve. As total pressure distortion amplification also depends on the slope of the pressure ratio curve, the static pressure distortion at the rotor exits will often be in phase with the total pressure distortion under conditions which would amplify the total pressure distortion and out of phase under conditions which would attenuate the total pressure distortion. Since static pressure at the rotor exit is generally used as a boundary condition in rotor calculations, the existence of the static pressure distortions mentioned above is an issue for calculations involving rotors subjected to inlet distortions. The outflow boundary must be placed sufficiently far downstream (more than one compressor diameter downstream) for the static pressure non-uniformity associated with the distortion to decay to a negligible value.

Localized swirl at the rotor inlet is demonstrated using the results from the Stage 35 model. This swirl is the response of the flow to a static pressure non-uniformity induced by the rotor. The static pressure distortion at the rotor inlet may or may not be in phase with the static pressure distortion at the rotor exit. Its strength and phase depend on compressor inlet geometry and compressor performance in response to distorted flow. Localized swirl adds to the incident angle non-uniformity caused by the distortion in velocity. The existence and effects of localized swirl could not be studied in any considerable detail with the ADLARF data set, as the only data taken near the rotor inlet were of static pressure on the hub and casing.

6.1.2 Compressor Performance

Comparison of clean and distorted experimental performance parameters show that the distortion causes minimal change in ADLARF total pressure and temperature ratios despite a shift in the operability range. An improvement in stall margin is also observed for the distorted flow.

The unsteadiness of the distorted flow, as indicated by its reduced frequency, may be responsible for minimizing losses and improving stall margin. Losses, which could occur in distorted flow segments if the flow were steady, may not have time to manifest themselves before the flow changes. The result is minimal degradation in performance despite local operation outside the clean flow operability range. To this extent, reduced frequency (which is a measure of time spent in each distorted segment) and distortion amplitude may be important parameters regarding compressor performance under total pressure distortions.

Performance parameters from the RANS computation of the ADLARF first rotor were compared to the measured parameters for Rotor 1 in distorted flow. The model predicts average pressure and temperature ratios to within one or two percent but over-predicts efficiency by approximately nine percent. As mentioned in Section 6.1.1 above, the model also over-predicts distortion amplification by a factor of four.

6.1.3 Blade Aerodynamics and Structural Response

Both the experimental (LDV) and computational (RANS) blade passage data show that the blade passage flow field fluctuates in response to the distorted flow. There is fluctuation in the size of the transonic (LDV) and supersonic (RANS) regions near the suction-side leading edge. There is also the appearance and disappearance of a high-speed stream along the pressure-surface in the LDV data, of a pitch-wise strip of low-speed flow near the exit of the blade passage in the LDV data, and of a weak blade passage shock in the computational data. Neither the LDV nor the computational data set, however, is a perfect match for the ADLARF rake and blade data. The LDV data are at a lower compressor speed than the rake and blade data, and the RANS rotor computation uses a smaller amplitude total pressure distortion (Figure 3-6) than is reflected in the experimental data (Figure 3-5).

Kulite data along the 85% span show deviations in both amplitude and phase progression in the first third of the chord for one of two blades instrumented in the distorted flow case. This may indicate that the flow in that region on that particular blade is cycling between being separated and attached to the blade. Even though the RANS rotor computation did not reflect separation, separation may still have occurred in the experiment—the inlet distortion imposed in the experiment had a larger amplitude than that imposed in the rotor computation. In addition to deviations in 3/rev pressure amplitude and phase along the chord, the kulite data show some blade-to-blade variations in both the clean and distorted flow.

Fourier decomposition of the blade force calculated from the kulite measurements shows some low amplitude, low frequency components in addition to the dominant 3/rev distortion component. Decomposition of blade strain shows an almost exclusive 3/rev response. This is likely due to the proximity of the forcing frequency to resonance as well as the location of the strain gauge at that resonance mode's bending location. Both blade force and blade strain show blade-to-blade variations.

Phase comparisons of blade strain on five adjacent blades shows that the blades are responding near the 3/rev interblade phase angle. The phase difference between the forces on two adjacent blades, however, is not near the interblade phase angle. This may suggest that a 16-blade oscillation mode is excited for the distorted flow case or that the measured blade force is not representative of the total force on the blade.

Blade-to-blade variability in response-to-force ratios is greater for the clean flow case than for the distorted flow case. This could mean that, in distorted flow, adjacent blades are coupled, adding to the plausibility of a 16-blade oscillation mode. On the other hand, if the measured blade force does not accurately represent the total force on the blade, such a conclusion may be in error.

Phase differences between force and response appear to indicate that the individual blades are not oscillating as linear, second-order systems. This may also support the plausibility of a 16-blade oscillation mode; but, again, accurate representation of the blade force is an issue in obtaining accurate force and response phasing.

6.2 Experimental Issues

In the course of seeking answers to the questions posed in Chapter 1, several issues became evident regarding the use of experimental data. They are as follows:

(1) Sign convention. In Section 5.2.5, a sign convention had to be assumed for the strain gauge measurements, resulting in uncertainty in making phase comparisons with the measured blade force.

(2) Number of blades instrumented. Increasing the number of instrumented blades could add an element of repeatability as well as pick up patterns in blade-to-blade variability.

(3) Blade force representation. Measurements taken at the 85% span of a blade may or may not be representative of the integrated force on the blade.

(4) Measurement synchronization. Accurate synchronization of all measurements is essential for characterizing transient events.

(5) Repeatability and uncertainty in the data. This analysis of the ADLARF data was made without information regarding repeatability or uncertainty.

6.3 Conclusions

The following conclusions can be inferred from this research:

1. The ADLARF compressor rotors amplify the distortion.

2. The compressor rotors behave as low-pass filters because the blades tend to respond to an average of the higher frequency pressure fluctuations along the blade. Results show that an appropriate length scale for low-pass corner frequency for low-aspect-ratio blades is one-half the blade chord. The physical reason for this is that most of the work done on the flow is done in the first half of the chord.

3. The change in performance when the ADLARF compressor is subjected to the 3/rev sinusoidal distortion is minimal. The observed improvement in compressor stall margin is potentially due to the unsteadiness of the flow—resident time in flow segments outside the clean flow operability range may be too short to allow the establishment of loss mechanisms.

4. The 3/rev distortion may excite a 16-blade resonance mode in the rotor—it is unknown whether the blade-to-blade coupling would be mainly through the blade passage aerodynamics, mainly through the disk, or have comparable contributions from both.

6.4 Future Work

This research results from the first collaboration between AFRL-WPAFB, GEAE, NASA-GRC, and the MIT-GTL. From the MIT-GTL standpoint, the most important and intangible achievement of this effort has been the familiarization with collaborators' resources, research problems, and research interests. In addition to identifying future tasks, this research has served to identify how best to utilize this collaboration in the future.

The present effort constitutes an initial attempt at a university-government-industry research partnership involving the MIT Gas Turbine Laboratory, AFRL-WPAFB, NASA-GRC, and GEAE on a problem of relevance to the operability and durability of aircraft turbine engines. In order for research of this nature to impact turbomachinery design, links must be made between computations and testing and between ground tests and in-flight tests. The following tasks could potentially contribute to establishing those links:

(1) Use computational fluid dynamics to determine locations of kulite sensors for more useful blade force representation.

(2) Investigate the coupling mechanism. When excited near resonance blades appear to be coupled to one another—mechanically, aerodynamically or both.

(3) Investigate reduced frequency trends. Reduced frequency likely plays a role in both distortion propagation (low-pass corner frequency) and compressor performance (stall margin).

(4) Extend the RANS rotor calculation to model annulus geometry between the compressor inlet measurement station (approximately one rotor radius upstream of the rotor inlet) and the Stator 1 leading edge measurement station. This will ensure that the calculation has the same boundary conditions (especially upstream) as the rotor in the experiment so that direct comparisons can be made between computation and experiment.

(5) Investigate how to set exit boundary conditions for effective single rotor calculations involving distorted flow.

(6) Adapt Gong model [12] for the ADLARF compressor to enable performance prediction for distorted flow.

(7) Compare in-flight measurements of turbulence to the turbulence generated by the distortion screen.

The process of this research has yielded some lessons learned regarding how to make the best use of the collaboration. As the process must be paced to the learning curve of a new research assistant, the following recommendations and schedule result:

1. Orientation period. Advisor provides research assistant with a copy of the original proposal or statement of work and educates him/her in the new field.

2. Planning meeting with collaborators. Collaborators present their perspective and past work on the research topic. Research assistant and advisor present research plan and work out details and logistics with collaborators. This meeting determines the scope and timeline of the project, the data/experiments to be used, relevant literature to be provided, and the technical conference to which the work applies.

3. Attendance of relevant conference in the early stages of the research effort. Research assistant attends relevant sessions and interfaces with the collaborators and other leaders in the field.

4. Mid-term report. Research assistant provides report and status to the collaborators—opportunity for feedback and modification of the research plan. All results, data, and literature shall have been sent to the research assistant by this time.

5. Presentation of results to collaborators. All analysis shall be complete by this time.

6. Conference presentation. Research assistant presents work to the professional community, interfaces with the collaborators and other leaders in the field.

7. Completion of thesis. Early completion may be necessary to ensure perusal by government document control authorities.

The above recommendations and schedule aim to do the following:

(a) Provide the research assistant with intangible yet important perspective early in the process—this shall enable more self-determination earlier on in the process.

(b) Involve collaborators more in the planning and process of the research—this shall ensure relevance of the project and the full engagement of the collaborators.

(c) Provide deadlines that ensure optimal use of time and resources—this shall ensure efficient use of time and emphasize quality over quantity.

BIBLIOGRAPHY

[1] Manwaring, S. R., Rabe, D. C., Lorence, C. B., and Wadia, A. R., "Inlet Distortion Generated Forced Response of a Low-Aspect-Ratio Transonic Fan," *ASME Journal of Turbomachinery*, Vol. 119, pp. 665-676 (1997)

[2] Cybik, B. Z., Rabe, D. C., Russler, P. M., and Hah, C., "Characterization of the First-Stage Rotor in a Two-Stage Transonic Compressor," AIAA-95-2460 (1995)

[3] Hah, C., Rabe, D. C., Sullivan, T. J., and Wadia, A. R., "Effects of Inlet Distortion on the Flow Field in a Transonic Compressor Rotor," ASME 96-GT-547 (1996)

[4] Minkiewicz, G., and Russler, P. M., "Unsteady Aerodynamics in Transonic Compressor Rotor Blade Passages" AIAA-98-3897 (1998)

[5] Marshall, J. G., Chew, J. W., and Lee, S. J., "Forced Response Study of Distortion Driven Resonance in a Low Aspect Ratio Fan," Rolls-Royce white paper

[6] Bolcs, A., "ADLARF Blade Kulite Measurements," Virginia Polytechnic Institute and State University technical report (1993)

[7] Rabe, D. C., Bolcs, A., and Russler, P. M., "Influence of Inlet Distortion on Transonic Compressor Blade Loading," AIAA-95-2461 (1995)

[8] Kenyon, J. A., Rabe, D. C., and Fleeter, S., "Aerodynamic Effects on Blade Vibratory Stress Variations," AIAA-98-3744 (1998)

[9] Kenyon, J. A., and Fleeter, S., "Aerodynamic Effects on Mistuned Response of a High-Speed, Low Aspect Ratio Fan," AFRL-PR-WP-TR-1998-2118 (1998)

[10] Kenyon, J. A., "Robust Maximum Forced Response in Mistune Turbine Engine Bladed Disks," Ph.D. Dissertation, Carnegie Mellon University (2002)

[11] Woehr, D. A., and Manwaring, S. R., "Augmented Damping of Low Aspect Ratio Fans," WL-TR-95-2008 (1995)

[12] Gong, Y., "A Computational Model for Rotating Stall and Inlet Distortions in Multistage Compressors," MIT GTL Report #230 (1999)

[13] Greitzer, E. M., "Inlet Distortion Effects in Axial Compressors," Von Karman Institute Lecture Series *Unsteady Flow in Turbomachinery* (1979)

[14] Greitzer, E. M., and Tan, C. S., *Internal Flows*, Section 6.3 (To Appear)

[15] Roach, P. E., "The Generation of Nearly Isotropic Turbulence by Means of Grids," *International Journal of Heat and Fluid Flow*, Vol. 8, No. 2, pp. 82-92 (June 1987)

APPENDICES

A TURBULENCE LENGTH SCALES FOR THE DISTORTION SCREEN

Roach [15] presents the theoretical and empirical bases for determining turbulence parameters for turbulence generated by grids positioned normal to uniform flows with low background turbulence. This appendix summarizes these bases and uses them to make length scale calculations for the ADLARF distortion screen.

A-1 Theory

The theoretical equations set forth for the length scales assume that the turbulence is isotropic, that is that

$$\lambda_y \equiv \lambda_z = \frac{\lambda_x}{\sqrt{2}}$$

where λ_y, λ_z, and λ_x are the micro-scale components, and

$$\Lambda_y \equiv \Lambda_z = \frac{\Lambda_x}{2}$$

where Λ_y, Λ_z, and Λ_x are the macro-scale components. (Experiments tend to confirm the assumption of isotropy.) Furthermore, the equations are derived from the relationship between the micro-scale and the turbulence decay rate,

$$\frac{d\overline{u^2}}{dt} = -10\nu \frac{\overline{u^2}}{\lambda_y^2}$$

where u^2 is the x-component of the mean square fluctuating velocities, t is time, and ν is the fluid kinematic velocity. From the definition of the x-component turbulence intensity,

$$T_u = \frac{\sqrt{\overline{u^2}}}{U}$$

where U is the mean flow velocity (in the x-direction). With the knowledge that

$$t = \frac{x}{U}$$

the relationship between the micro-scale and the turbulence decay rate can be manipulated to yield

$$\left(\frac{\lambda_x}{d}\right)^2 = \frac{-10T_u}{R_d}\left[\frac{dT_u}{d(x/d)}\right]^{-1}$$

where d is the grid wire diameter and

$$R_d = \frac{Ud}{\nu}$$

is the Reynolds number. For high Reynolds number flows,

$$T_u = C\left(\frac{x}{d}\right)^{-5/7}$$

where C is a constant, and

$$\left(\frac{\lambda_x}{d}\right)^2 = \frac{14F}{R_d}\left(\frac{x}{d}\right)$$

$$\left(\frac{\lambda_y}{d}\right)^2 = \frac{7G}{R_d}\left(\frac{x}{d}\right)$$

$$\left(\frac{\lambda_z}{d}\right)^2 = \frac{7H}{R_d}\left(\frac{x}{d}\right)$$

where F, G, and H are constants which equal one if the turbulence is truly isotropic.

To get growth rate equations for the macro-scale, the author assumes and references other work that supports that the macro-scale growth rate is proportional to the micro-scale growth rate. This assumption can also be supported using the definition of the streamwise micro-scale,

$$\frac{1}{\lambda_x^2} = \frac{-1}{2U^2}\left[\frac{\partial^2 R(T)}{\partial T^2}\right]_{T=0}$$

where *R(T)* is the autocorrelation function

$$R(T) = \frac{\overline{u(t)u(t-T)}}{\overline{u^2}}$$

and T is the autocorrelation time delay. If the turbulence is truly isotropic and homogeneous and the velocity field is uniform, a first approximation of *R(T)* is

$$R(T) = e^{-UT/\Lambda_x}$$

Substituting this approximation into the definition of the streamwise microscale,

$$\Lambda_x^2 = \frac{-\lambda_x^2}{2}$$

While this result demonstrates the inadequacy of the above approximation of *R(T)* for relating λ_x and Λ_x, it does support the assumption of proportional macro-scale growth. The equations set forth for the macro-scale are therefore

$$\frac{\Lambda_x}{d} = I\sqrt{\frac{x}{d}}$$

$$\frac{\Lambda_y}{d} = \frac{IJ}{2}\sqrt{\frac{x}{d}}$$

$$\frac{\Lambda_z}{d} = \frac{IK}{2}\sqrt{\frac{x}{d}}$$

where I, J, and K are constants, with J and K equal to one if the turbulence is truly isotropic. The Reynolds number dependence of the micro-scale has been removed since there is no theoretical or empirical evidence of it in the macro-scale for the Reynolds range of interest.

A-2 Empirical Equations

The empirical equations for the micro-scale are as follows:

$$\left(\frac{\lambda_x}{d}\right)^2 = \frac{17.0}{R_d}\left(\frac{x}{d}\right)$$

$$\left(\frac{\lambda_z}{d}\right)^2 = \frac{8.5}{R_d}\left(\frac{x}{d}\right)$$

$$\left(\frac{\lambda_y}{d}\right)^2 = \frac{8.5}{R_d}\left(\frac{x}{d}\right)$$

The relationship between the x-component constant and the y- and z-component constants confirm the assumption of isotropy. The fact that the constants are scaled slightly from the theoretical equations is not unusual since measuring turbulence accurately is very difficult.

The empirical equations for the macro-scale are as follows:

$$\frac{\Lambda_x}{d} = .20\sqrt{\frac{x}{d}}$$

$$\frac{\Lambda_y}{d} = .10\sqrt{\frac{x}{d}}$$

$$\frac{\Lambda_z}{d} = .10\sqrt{\frac{x}{d}}$$

Again, the values of the constants confirm the assumption of isotropy.

A-3 Calculations

An educated guess was made at the grid sizes of the 3/rev distortion screen in the ADLARF tests. The largest grid sizes were assumed to be no more than .28"×.28" with round wire diameters of .04"; the smallest grid sizes were assumed to be no less than .04"×.04" with round wire diameters of .01". The Reynolds numbers based on the wire diameters for the largest and smallest grid sizes were calculated as follows:

$$(R_d)_{l\arg e} = \frac{\rho U d}{\mu} = \frac{.0767\,lbm/ft^3(288\,ft/s)(.04')}{1.84\times10^{-5}\,lbm/ft\cdot s}\left(\frac{ft}{12"}\right) = 4001$$

$$(R_d)_{small} = (R_d)_{l\arg e}\times\left(\frac{.01"}{.04"}\right) = 1000$$

For the purposes of future comparisons with flight data, downstream distances of 56" and 70.6" were also used to set the limits on a range for the length scales.

That the micro-scales are dependent on Reynolds number is not exactly true since the wire diameter drops out of the equations. (Wire diameter was added to the micro-scale growth rate equations in the first place in order to construct the Reynolds number.) The resulting micro-scales are calculated as follows:

$$(\lambda_x)_{x=56"} = \sqrt{\frac{17xd}{R_d}} = \sqrt{\frac{17x\mu}{\rho U}} = \sqrt{\frac{17(56")(1.84\times10^{-5}\,lbm/ft\cdot s)}{.0767\,lbm/ft^3(288\,ft/s)}\left(\frac{12"}{ft}\right)} = .098"$$

$$(\lambda_x)_{x=70.6"} = (\lambda_x)_{x=56"}\times\sqrt{\frac{70.6"}{56"}} = .11"$$

$$(\lambda_y)_{x=56"} = (\lambda_z)_{x=56"} = \frac{(\lambda_x)_{x=56"}}{\sqrt{2}} = .069"$$

$$(\lambda_y)_{x=70.6"} = (\lambda_z)_{x=70.6"} = \frac{(\lambda_x)_{x=70.6"}}{\sqrt{2}} = .078"$$

The macro-scales are dependent on wire diameter, and the calculations are as follows:

$$((\Lambda_x)_{x=56"})_{l\arg e} = .2\sqrt{xd} = .2\sqrt{56"(.04")} = .3"$$

$$((\Lambda_x)_{x=56"})_{small} = .2\sqrt{56"(.01")} = .15"$$

$$((\Lambda_x)_{x=70.6"})_{l\arg e} = .2\sqrt{70.6"(.04")} = .34"$$

$$((\Lambda_x)_{x=70.6"})_{small} = .2\sqrt{70.6"(.01")} = .17"$$

$$\left(\left(\Lambda_y\right)_{x=56"}\right)_{large} = \left(\left(\Lambda_z\right)_{x=56"}\right)_{large} = \frac{\left(\left(\Lambda_x\right)_{x=56"}\right)_{large}}{2} = .15"$$

$$\left(\left(\Lambda_y\right)_{x=56"}\right)_{small} = \left(\left(\Lambda_z\right)_{x=56"}\right)_{small} = \frac{\left(\left(\Lambda_x\right)_{x=56"}\right)_{small}}{2} = .075"$$

$$\left(\left(\Lambda_y\right)_{x=70.6"}\right)_{large} = \left(\left(\Lambda_z\right)_{x=70.6"}\right)_{large} = \frac{\left(\left(\Lambda_x\right)_{x=70.6"}\right)_{large}}{2} = .17"$$

$$\left(\left(\Lambda_y\right)_{x=70.6"}\right)_{small} = \left(\left(\Lambda_z\right)_{x=70.6"}\right)_{small} = \frac{\left(\left(\Lambda_x\right)_{x=70.6"}\right)_{small}}{2} = .085"$$

The lowest frequency associated with these turbulence length scales was determined from the largest macro-scale and calculated as follows:

$$f = \frac{U}{(\Lambda)_{\max}} = \frac{288\, ft/s}{.34"}\left(\frac{12"}{ft}\right) = 10{,}200Hz$$

A-4 Conclusions

Based on the above calculations and assumptions of grid dimensions, the range in micro-scales is .098” to .11” in the flow direction and .069” to .078” perpendicular to the flow; the range in macro-scales is .15” to .34” in the flow direction and .075” to .17” perpendicular to the flow, and the lowest frequency associated with these length scales is 10,200 Hz.

B TIME-SCALE CALCULATIONS FOR ROTATING DISTORTION SCREEN

B-1 Time Scales

B-1.1 Distortion Rotation

The time scale for the rotation of the distortion is

$$\tau_d = \frac{\theta_d}{f_s} = \frac{120^\circ}{2^\circ / s} = 60s$$

where θ_d is the angular wavelength of the distortion and f_s is the distortion screen rotation frequency.

B-1.2 Downstream Convection

The time scale for the convection of flow from the distortion screen to the compressor inlet is

$$\tau_c = \frac{l_i}{U_o} = \frac{56"}{288 ft / s} \times \frac{ft}{12"} = .0162s$$

where l_i is the distance between the distortion screen and compressor inlet and U_o is the average flow velocity at the bellmouth.

B-2 Conclusion

Comparison of the above time scales reveals that the distortion screen barely rotates during the time it takes for the flow to get from the distortion screen to the compressor inlet. Therefore, the distorted flow can be considered quasi-steady.

C FLOW FIELD DATA SOURCES

C-1 Measurement Locations

Note that data from several sensors are missing. One rotor diameter is 27.75 inches.

C-1.1 Flow Conditioning Barrel

Barrel Diameter: 10 ft

Axial Location: 9.3 rotor diameters in front of the Rotor 1 leading edge

Measurements:

Total Temperature (TT00). Forty-eight thermocouples spaced across the flow on the final flow conditioning element.

C-1.2 Bellmouth

Bellmouth Radius: 13.875 in

Axial Location: 2.82 rotor diameters in front of the Rotor 1 leading edge

Measurements:

Total Pressure (PT10) and Differential Pressure (PT10-PS10). Four rakes with pitot sensors at 0, 90, 172, and 285 degrees from top dead center, aft looking forward. Six sensors per rake at 13.281, 12.006, 10.581, 8.933, 6.903, and 3.956 inches from the compressor center line.

C-1.3 Compressor Inlet

Inlet Radius: 13.875 in

Axial Location: .524 rotor diameters in front of the Rotor 1 leading edge

Measurements:

Static Pressure (PS15). Eight sensors about the inlet circumference. The sensors are located at 45-degree increments, starting at 15 degrees from top-dead-center, aft looking forward.

Total Pressure (PT15). Eight rakes located at 45-degree increments, starting at 5 degrees from top-dead-center, aft looking forward. Five sensors per rake at 13.135, 11.565, 9.765, 7.545, and 4.305 inches from the compressor center line.

C-1.4 Rotor 1 Leading Edge

Outer Radius: 13.875 in

Measurements:

Static Pressure (PSR1L). Seven sensors about the outer circumference at 0, 45, 90, 139, 180, 225, and 270 degrees from top-dead-center, aft looking forward.

C-1.5 Stator 1

Inner Radius: 8.739 inches at the leading edge and 9.813 inches at the trailing edge

Outer Radius: 13.875 in

Hub Axial Location: from 6.436 to 9.925 inches downstream of the Rotor 1 leading edge

Tip Axial Location: from 7.023 to 9.98 inches downstream of the Rotor 1 leading edge

Measurements:

Leading Edge Static Pressure (PSS1L). Three sensors about the hub circumference and three sensors about the casing circumference at 63, 184, and 272 degrees from top-dead-center, aft looking forward.

Leading Edge Total Pressure (PTS1L) and Total Temperature (TTS1L). Three radial arrays at 52, 176, and 289 degrees from top-dead-center, aft looking forward. Seven sensors per array at approximately 9.3, 9.6, 10.3, 11.3, 12.3, 13.2, and 13.5 inches from the compressor center line. (The arrays did not have the exact same radial locations for the sensors.)

Hub and Tip Static Pressure (PSS1). Three hub arrays starting at 63.1, 186, and 273.8 degrees from top-dead-center, aft looking forward, and three tip arrays starting at 65.4, 188.3, and 276.1 degrees from top-dead-center, aft looking forward. Each array has five sensors following the sweep of the blade.

Trailing Edge Static Pressure (PSS1T). Three sensors about the hub circumference and three sensors about the tip circumference at 68, 189, and 278 degrees from top-dead-center, aft looking forward.

C-1.6 Rotor 2 Tip

Outer Radius: 13.875 in

Axial Location: from approximately 10.3 to 12.667 inches downstream of the Rotor 1 leading edge

Measurements:

Static Pressure (PSR2). An axial array of ten sensors along the outer wall at 41 degrees from top-dead-center, aft looking forward.

C-1.7 Stator 2

Inner radius: 11.07 inches at the leading edge and 11.16 inches at the trailing edge

Outer radius: 13.875 inches at the leading edge and 13.606 inches at the trailing edge

Hub axial location: from 13.16 to 15.291 inches downstream of the Rotor 1 leading edge

Tip axial location: from 12.995 to 15.571 inches downstream of the Rotor 1 leading edge

Measurements:

Leading Edge Static Pressure (PSS2L). Three circumferential arrays about the hub circumference and three about the tip circumference. Each array has five equally spaced sensors spanning 6 degrees. The hub arrays start at 28, 159, and 287 degrees from top-dead-center, aft looking forward. The tip arrays start at 12, 159, and 287 degrees from top-dead-center, aft looking forward.

Leading Edge Total Pressure (PTS2L) and Total Temperature (TTS2L). Three radial arrays at 36, 168, and 276 degrees from top-dead-center, aft looking forward. Seven sensors per array at 13.604, 13.396, 12.972, 12.396, 11.864, 11.445, and 11.225 inches from the compressor center line.

Trailing Edge Static Pressure (PSS2T). Three sensors about the hub circumference and three sensors about the tip circumference at 31, 162, and 297 degrees from top-dead-center, aft looking forward.

C-1.8 Compressor Exit

Inner Radius: 10.96 inches at 16.22 inches downstream of the Rotor 1 leading edge

Outer Radius: 13.48 inches at 16.7 inches downstream of the Rotor 1 leading edge

Axial Location: 15.91 inches downstream of the Rotor 1 leading edge and beyond

Measurements:

Circumferential Static Pressure (PS23O). Seven sensors about the hub circumference at 16.22 inches downstream of the Rotor 1 leading edge and seven sensors about the outer circumference at 16.7 inches downstream of the Rotor 1 leading edge. The hub sensors are at 26, 83, 122, 171, 231, 297, and 331 degrees from top-dead-center, aft looking forward, and the casing sensors are at 39, 99, 165, 199, 254, 311, and 350 degrees from top-dead-center, aft looking forward.

Axial Static Pressure (PS23). An axial array of six sensors along the outer wall at 165 degrees ranging from 15.91 to 20.275 inches downstream of the Rotor1 leading edge and an axial array of seven sensors along the hub at an undocumented location.

Total Pressure (PT23) and Total Temperature (TT23). Seven arc rakes with radial locations ranging from 11.215 to 13.229 inches from the compressor center line and axial locations ranging from 16.255 to 16.671 inches downstream of the Rotor 1 leading edge. The arc rakes are centered at 270, 174, 0, 270, 174, 0, and 90 degrees.

C-2 OTHER MEASUREMENTS AT EACH TIME STEP

Mechanical rotation speed of the rotor (N)
Rotation angle of the distortion screen (SCRNANG)
Stator 1 vane position (S1POS)

C-3 CALCULATIONS PROVIDED AT EACH TIME STEP

Percent corrected speed (PNC2)
Corrected rotor speed (NC2)
Corrected mass flow rate (WAV31C)
Overall total temperature ratio (TR)
Overall total pressure ratio (PR)
Overall efficiency (ETA)
Stage 1 total pressure ratio (PRS1)
Stage 1 total temperature ratio (TRS1)
Stage 1 efficiency (ETAS1)

Average bellmouth total pressure (PT10)
Average Stator 1 leading edge total pressure (PTS1)
Average Stator 1 leading edge total temperature (TTS1)

D PARALLEL COMPRESSOR THEORY FOR COMPRESSIBLE FLOWS

In his Von Karmen Institute lecture [13], Greitzer presented parallel compressor theory that included a brief description for compressible flow. This appendix fills in the theory about distortion amplification for compressible flow, addresses static pressure nonuniformities downstream of the rotor, and presents a modified version of compressor performance prediction.

D-1 Assumptions

1. The flow in each of the parallel compressors must be uniform. As can be seen in Figure 3-5, the distortion yields a sawtooth total pressure distribution. The only way to model performance using the parallel compressor method is to either slice the flow up into infinitisimal uniform flow parallel compressors or to turn the sawtooth pattern into an average uniform distortion pattern. The latter approach was taken as an approximation in this analysis. The problem that remains in modeling performance for a 3/rev sinusoidal (or sawtooth) distribution is that the blade response is not really quasi-steady (Section 4.2.2), which is what parallel compressor theory assumes in using the clean flow performance curves.

2. Negligible circumferential flow redistribution within the compressor. This implies the presence of inlet guide vanes, which is not the case for the data in this thesis. Flow redistribution is seen in Figure 3-13 for the NASA Stage 35 compressor. There is most likely similar local swirl induced in the ADLARF compressor due to static pressure distortions. Parallel compressor predictions will be less accurate if there is flow redistribution than if there is no flow redistribution, but the predictions should still be qualitatively correct.

D-2 Theory

In general, parallel compressor theory assumes that a compressor will have the same effect on a segment of uniform (total pressure) flow as it will on a full uniform flow of the same properties. The two main predictions the theory is responsible for are distortion amplification and mean compressor performance. The theory for these two predictions is presented as well as some theory on static pressure distortions.

D-2.1 Distortion Amplification

Prediction of distortion amplification is actually more straightforward for compressible flow than for incompressible flow because the performance curves are in pressure ratios. It is as simple as taking the corrected mass flow rate for each uniform flow segment, extrapolating each flow rate to that for the total flow area, and mapping the extrapolated flow rates to their respective pressure ratios. For a distortion with uniform high- and low-speed segments, the predicted distortion amplitude is:

$$p_{t2H} - p_{t2L} = \pi_H p_{t1H} - \pi_L p_{t1L}$$

where p_t corresponds to total pressure, π corresponds to pressure ratio, the subscripts *1* and *2* correspond to the compressor or stage inlet and exit, respectively, and the subscripts *H* and *L* correspond to the high- and low-speed flow segments, respectively. It should be clear that, if the pressure ratio is significantly higher for the low-speed flow than for the high-speed flow (i.e., steep negative pressure ratio curve slope), the distortion will be attenuated. Conversely, the distortion will be amplified if the pressure ratio curve has a steep positive slope—although this is never the case as the compressor would be unstable.

The transition between amplification and attenuation is not so clear, however, from the equation above. The following modification of the equation,

$$\frac{p_{t2H} - p_{t2L}}{\overline{p_{t2}}} = \frac{\pi_H p_{t1H} - \pi_L p_{t1L}}{\overline{\pi p_{t1}}}$$

combined with some logic in the paragraph below will make the transition clear. The overbars in the denominators indicate area averages. Area averages are chosen here because measurements taken across an annulus lend themselves to area-averaging. Mass-averaging would be necessary for computing average work done on the flow.

Using the modified equation, start with a flat pressure ratio curve. The pressure ratios cancel out. There is no amplification or attenuation of the distortion amplitude as a percentage of its local average. Now leave everything else the same—same inlet distortion, same average pressure ratio, and, hence, same average total pressure at the exit—but let the the pressure ratio curve have a negative slope to it. The pressure ratio for the high-speed flow is less than what it was when the curve was flat, and the pressure ratio for the low-speed flow is now higher than it was before. Hence, the first term in the right-hand-side numerator is less than it was before, and the second term in the numerator is greater than it was before. The term on the left-hand-side is then less than it was before and less than the incident distortion amplitude as a percentage of its local average. The distortion amplitude, as a percentage of its local average, has been attenuated. In a similar manner, a positive-sloped pressure ratio curve can be shown to amplify the distortion amplitude as a percentage its local average.

D-2.2 Static Pressure Distortions

Static pressure distortions are linked with performance curves and total pressure distortion amplification. They are created by the geometry changes within the compressor as it pumps distorted (total pressure) flow from a uniform static pressure field far upstream to a uniform static pressure field far downstream. To summarize for cases of minimal flow redistribution, if the area at the exit (inlet) measurement station is less than that at the uniform static pressure plane far downstream (upstream), the static pressure distortion at the measurement station will be out of phase with the total pressure distortion. If the area at the exit (inlet) measurement station is larger than that at the uniform static pressure plane far downstream (upstream), the static pressure distortion at the measurement station will be in phase with the total pressure distortion. Thus, geometry is involved in setting the static pressure boundary conditions for rotors. This sub-section shows how the static pressure boundary condition at the rotor or compressor exit is coupled to rotor or compressor performance.

Pressure ratio curves used for compressible flow predictions give limited insight into static pressure. For this reason, a total-to-static pressure rise curve, which is more appropriate for incompressible flow predictions, is used to facilitate a qualitative understanding of static pressure distortions downstream of rotors. For simplicity, the rotor specific dynamic pressure, which is typically used to normalize the total-to-static pressure rise, is left out.

The difference between the total-to-static pressure rise due to a low total pressure flow segment and that due to a high total pressure segment can be defined as:

$$\Delta = (p_{2L} - p_{t1L}) - (p_{2H} - p_{t1H})$$

Rearranging terms yields the static pressure amplitude:

$$(p_{2H} - p_{2L}) = (p_{t1H} - p_{t1L}) - \Delta = (p_{t1H} - p_{t1L})\left[1 - \frac{\Delta}{(p_{t1H} - p_{t1L})}\right]$$

Since the total pressure amplitude is proportional to the distorted flow coefficient amplitude,

$$(p_{2H} - p_{2L}) = (p_{t1H} - p_{t1L})(1 + Cb)$$

where b is the slope of a line drawn between the two performance points and C is a positive coefficient that most likely adds non-linearity to the equation. Still, it is evident that the static pressure distortion at the exit measurement station will be out of phase with the total pressure distortion if the total-to-static pressure rise curve has a steep negative slope and in phase with the total pressure distortion if the slope is nearly flat or positive. Thus, the static pressure distortion will likely be out of phase with the total pressure distortion if the total pressure distortion is attenuated and in phase if the total pressure distortion is amplified.

D-2.3 Overall Performance

Prediction of compressor performance is an area average of the performance of the high and low total pressure flow segments:

$$\overline{p_{t2}} = \frac{\pi_H p_{t1H} A_H + \pi_L p_{t1L} A_L}{A_{H+L}} = \overline{\pi p_{t1}}$$

These are the same performance mappings used in the distortion amplification analysis in Section D-2.1.

4760
63